

H₂CO and H_{110 α} observations towards NH₃ sources

Ye Yuan^{1,2} • Jarken Esimbek^{1,3} • Jian Jun Zhou^{1,3}
• Xin Di Tang^{1,2} • Gang Wu^{1,2,3} • Ying Xiu Ma^{1,3}

Abstract We observed the H₂CO (1₁₀ – 1₁₁) absorption lines and H_{110 α} radio recombination lines (RRL) toward 180 NH₃ sources using the Nanshan 25-m radio telescope. In our observation, 138 sources were found to have H₂CO lines and 36 have H_{110 α} RRLs. Among the 138 detected H₂CO sources, 38 sources were first detected. The detection rates of H₂CO have a better correlation with extinction than with background continuum radiation. Line center velocities of H₂CO and NH₃ agree well. The line width ratios of H₂CO and NH₃ are generally larger than unity and are similar to that of ¹³CO. The correlation between column densities of H₂CO and extinction is better than that between NH₃ and extinction. These line width relation and column density relation indicate H₂CO is distributed on a larger scale than that of NH₃ and be in similar to the regions of ¹³CO. Abundance ratios between NH₃ and H₂CO were found to be different in local clouds and other clouds.

Keywords star formation; molecular cloud

Ye Yuan

E-mail: yuanye@xao.ac.cn

Jarken Esimbek

Jian Jun Zhou

Xin Di Tang

Gang Wu

Ying Xiu Ma

¹Xinjiang Astronomical Observatory, Chinese Academy of Sciences, Urumqi 830011, PR China.

²University of the Chinese Academy of Sciences, Beijing 100080, PR China.

³Key Laboratory of Radio Astronomy, Chinese Academy of Sciences, Urumqi 830011, PR China.

1 Introduction

Formaldehyde (H₂CO) and ammonia (NH₃) are good tracers of the physical conditions in galactic and extragalactic molecular clouds, such as density, temperature and kinematics (Mangum and Wootten 1993; Mangum et al. 2013). Both species have been detected in a wide range of dense interstellar environments. However, both of them suffer uncertainties caused by their formation mechanisms (Liszt et al. 2006). It is therefore of great interest to understand how these molecules are formed, evolve, and are related in the dense region. NH₃ is a common used and reliable temperature probe of molecular cloud (Walmsley and Ungerechts 1983; Wienen et al. 2012). The hyperfine satellite components can give optical depths, and the population of (1,1) and (2,2) can give an indication of the kinetic temperature. NH₃ emissions were widely detected in molecular clouds, both in dense cores (Myers and Benson 1983) and towards ultracompact HII regions (Churchwell et al. 1990). The typical environment parameters of NH₃ emissions are T_K ≥ 10 K and n(H₂) ≥ 10⁴ cm⁻³ (Ho and Townes 1983). The H₂CO absorption line was first detected in interstellar media by Snyder et al. (1969) and then collision cooling schemes of the doublet were developed (Snyder et al. 1969; Garrison et al. 1975). The scheme arrives at the lowest excitation temperature at a density region around 10⁴ cm⁻³ and would be quenched at the density larger than 10⁶ cm⁻³ (Garrison et al. 1975). This density range is expected to be higher than that of ¹²CO and comparable with that of ¹³CO and NH₃.

Few comparisons between these two tracers were made before. Scalise et al. (1981) observed NH₃ towards 35 strong H₂CO sources (the intensity of 6-cm absorption line is higher than 0.5 K) in the southern hemisphere. They reported 16 NH₃ detections and found no obvious statistical correlation between

the intensities of the two lines. Nash (1990) observed H_2CO and NH_3 in five clouds for their abundance ratios to restrict chemistry models, but they did not discuss the other parameters that the two spectres can probe. The abundance ratios of the two molecules $[\text{N}(\text{NH}_3)/\text{N}(\text{H}_2\text{CO})]$ they derived are mainly between 10 and 10^3 in different sources. Liszt et al. (2006) also discussed the abundance ratios of NH_3 and H_2CO in local diffuse clouds and got an abundance ratio $\langle \text{N}(\text{NH}_3)/\text{N}(\text{H}_2\text{CO}) \rangle \approx 0.4$.

The $\text{H}_2\text{CO}(1_{10} - 1_{11})$ transition and the $\text{NH}_3(1,1)$, (2,2) transitions are considered to be typical high density tracers in centimeter wavelength. Theoretical calculations and observations suggested that these transitions originated under similar environment conditions, but very few works have been done to investigate the relation between them directly. So we attempted to search H_2CO lines towards NH_3 sources and to search for potential relations between the two lines. In this paper, we present a new H_2CO absorption and $\text{H}_{110\alpha}$ emission survey toward 180 NH_3 sources. We seek the relation among the H_2CO , $\text{H}_{110\alpha}$ and NH_3 lines and make an analysis as regards the H_2CO absorption physical conditions affected by 6-cm continuum, infrared emission and extinction.

2 Observation and Data

2.1 Samples

The sources are selected from the following papers, and the types of sources and telescopes parameters are as follows:

1. MacDonald et al. (1981): UCHII regions, H_2O masers Herbig-Haro objects, reflection nebulae, CO 'hot spots' and HCN emission.
(Chilbolton 25-m, Beamwidth: 2.2')
2. Harju et al. (1993): IRAS sources in Orion and Cepheus molecular cloud.
(Effelsberg 100-m, Beamwidth: 40'')
3. Schreyer et al. (1996): Presumably massive young stellar objects, from bright 100 μm objects in IRAS Point Source Catalogue(PSC).
(Effelsberg 100-m)
4. Sridharan et al. (2002): Candidates of high-mass proto-stellar objects (HMPOs), chosen from IRAS-PSC with criteria: a.)detected in CS emission, b.)bright at FIR, c.)not detected in 6-cm continuum.
(Effelsberg 100-m)

The total number of the sources in the four papers is 218. Since our beam size of this observation is about

10', and to make sure the observation towards one source would not be interfered with other sources, we filtered part of the sources. Finally a list of 180 sources was used and every two sources in it are at least 10' apart. Among the 180 sources, 147 were detected to have $\text{NH}_3(1,1)$ emission lines in the four papers above. The line center velocities, line widths and column densities of NH_3 were used in the following discussions. The sources selected and their parameters are listed in Table 2, and the columns are as described in Section 3.

2.2 H_2CO and $\text{H}_{110\alpha}$ Observation

Observations of the $\text{H}_2\text{CO}(1_{10} - 1_{11})$ λ 6-cm absorption line ($\nu_0=4829.6594$ MHz) and $\text{H}_{110\alpha}$ RRL ($\nu_0=4874.1570$ MHz) have been made from September 2011 to August 2012, with the 25-m radio telescope of the Xinjiang Astronomical Observatory of Chinese Academy of Sciences. The telescope is located at Nanshan station (E87°10'40'', N43°28'22''). A dual-channel cooling receiver was used and provided a system temperature of ~ 23 K at zenith. A Digital Filter Bank (DFB) with 8192 channels was used. To observe H_2CO and $\text{H}_{110\alpha}$ RRL simultaneously, the center frequency of the spectrometer was set at 4851.9102 MHz. A 64 MHz bandwidth was used, resulting in a velocity resolution of 0.48 km s^{-1} . Two blocks of that in DFB with the same configuration were used simultaneously to process the two outputs of the receiver. The half-power beam width (HPBW) of the telescope is 9'.5 at this wavelength. The DPFU (Degrees Per Flux Unit) value was 0.116 K Jy^{-1} and the main beam efficiency at this wavelength is 65%. A noise-diode was used to calibrate the flux. The calibration of flux results in an error of about 10%. The observation was performed in position-switch mode. The on-source integration time of each source is 12 minutes, but for weak sources, we added observation time to make the signal-noise ratio above 3.

2.3 6-cm Continuum Data

*Sino-German 6 cm survey*¹ (Sun et al. 2007) data was used as T_C in Eq.2 to calculate the opacity. Of 180 selected sources 147 were located within the survey region and 33 were outside of that. For the sources not included in the survey, we observed 6-cm continuum with Nanshan 25-m radio telescope, using a cross-scan method with a bandwidth of about 400 MHz.

¹<http://zmtt.bao.ac.cn/6cm/>

2.4 Extinction Data

Extinction towards the sources was used to estimate the total H_2 column density, using the relation $N(H_2) = 0.94 \times 10^{21} A_V \text{ cm}^{-2}$ (Bohlin et al. 1978). The extinction data calculated from 2MASS by Dobashi (2011)² was used.

3 Results

Of the 180 sources observed, 138 sources are detected to have H_2CO lines and 36 to have $H_{110\alpha}$ RRL. 38 of the 138 detected H_2CO sources were new detections. Among the 36 RRL detections, 31 are consistent with H_2CO , and five sources have no H_2CO lines. The details are listed in Table.2. The columns are as follows:

1. -number
2. -source name
3. -right ascension of the source (J2000)
4. -declination of the source (J2000)
5. -extinction of Section 2.4
6. -6-cm continuum brightness temperature of Section 2.3, in T_{MB} scale
7. -the line center velocity of $NH_3(1,1)$
8. -the line width of $NH_3(1,1)$
9. -column density of NH_3 , in $(10^{13} \text{ cm}^{-2})$
10. -detection flag of $H_{110\alpha}$; 0 means not detected in observation, 1 means detected
11. -detection flag of H_2CO ; 0 means not detected in observation, 1 means detected, 2 means detected and newly detected
12. -reference.

The spectral lines were reduced using CLASS software³. For each source, all scans were averaged. Then a polynomial baseline was subtracted and gaussian fittings were made. Table.3 gives the fitting results. The columns are as follows: 1)-number; 2)-source name, the second, third and fourth velocity components are marked with b, c, and d if existing; 3)-LSR (Local Standard of Rest) velocity of line center and fitting error; 4)-peak intensity of H_2CO lines and fitting error; 5)-FWHM of line and fitting error; 6)-column density of H_2CO in 10^{13} cm^{-2} . For the sources with more than one velocity component, we assumed that the component the velocity of which is closest to the NH_3 velocity is associated with the NH_3 source, which was demonstrated to be reasonable by Kirk et al. (2007).

The column densities of H_2CO were derived using the formulation in Pipenbrink and Wendker (1988):

$$N(H_2CO) = 9.4 \times 10^{13} \tau_{peak} \cdot \Delta V \text{ (cm}^{-2}\text{)} \quad (1)$$

where τ_{peak} is the optical depth and ΔV is the line width. The constant 9.4×10^{13} has already been corrected for ortho-para ratio and rotational ladder for kinetic temperature at 10K.

Because the line widths of our sources are too large, the hyperfine structures (HFS) of $H_2CO(1_{10} - 1_{11})$ are blended and cannot be used to calculate the optical depth. We derived the optical depth through radiative transfer equation. The H_2CO apparent optical depth τ_{app} was determined through a simplified radiative transfer equation.

$$T_L = (T_{ex} - T_C - T_{CMB}) \times (1 - e^{-\tau_{app}}) \quad (2)$$

where T_L is the line brightness temperature, T_{ex} is the excitation temperature of this transition, T_C is the continuum brightness temperature, and T_{CMB} is the brightness temperature of the cosmic microwave background (CMB). The T_L and T_C values can be obtained through our observations directly, while the T_{ex} values are not clear to us. Several previous observations that can resolve the HFS of H_2CO reported that the T_{ex} values of this transition range from 1.5K to 2.0K (Heiles 1973; Vanden Bout et al. 1983; Young et al. 2004). So we assumed the T_{ex} value to be the mean value of what they reported, 1.7K. Also, we made RADEX (van der Tak et al. 2007) Non-LTE radiative transfer calculations to investigate the possible values of T_{ex} . The calculations show that the T_{ex} tends to be lower than the range above by about 0.5K and the consequent departure in column density will be less than half an order (see Appendix B), comparable with the uncertainty of the orth-para ratio estimated by Darling and Zeiger (2012). Besides, the T_{kin} used in the RADEX calculation is the temperature of NH_3 , which is the temperature of the center of the core and usually is higher than the average value across the core. So we may have overestimated the efficiency of the collision. The departures of T_{ex} and column density, indeed, should be smaller than the values estimated above.

4 Discussions

4.1 Influence of Extinction and Continuum Emission

The H_2CO detection rate of different extinction and continuum intervals are plotted in Fig.1. The detection rate monotonically increases with the increasing of

²<http://darkclouds.u-gakugei.ac.jp/2MASS/download.html>

³ CLASS is a part of GILDAS package, developed by IRAM (Institute de Radioastronomie Millimétrique). <http://www.iram.fr/IRAMFR/GILDAS/>

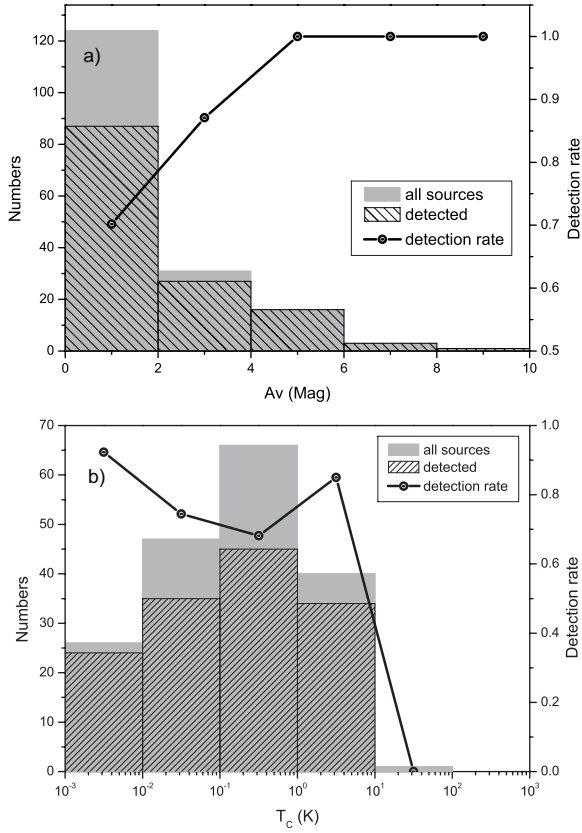


Fig. 1 Detection rate distribution of H_2CO . The *gray histogram* is the distribution of all the 180 selected sources in each a) extinction interval, b) continuum emission temperature interval. The *shaded histogram* is the distribution of sources detected H_2CO . The *solid line* is the detection rate, using the right axis.

extinction. The sources with extinction larger than 4 mag have 100% detection rate. All the 42 sources that did not detect H_2CO have the feature of low extinction. This suggests that the H_2CO absorption associates well with the dense region of the molecular clouds. Comparative studies of the H_2CO and ^{12}CO showed that the 4.8-GHz H_2CO absorption line is similar to the ^{12}CO , tracing the lower density region of the molecular cloud (Ridge et al. 2006; Zhang et al. 2012; Tang et al. 2013). This may indicate that the H_2CO absorption line can still probe the molecular cloud well, although it is believed sometimes to be dominated by background continuum radiation.

A high H_2CO detection rate of continuum sources (see Fig. 1.b)) indicates that the continuum emission strongly affects the H_2CO absorption line. The observation of Downes et al. (1980) and Zhang et al. (2012) showed that the H_2CO absorption line has a good correlation with the 6-cm continuum background. Toward

the continuum sources, the continuum radiation plays an important role in the determination of the H_2CO line intensity according to Eq.2. Therefore, the H_2CO absorption line intensities depend not only on the gas density, but also on the background continuum level.

The relation between detection rate and continuum brightness temperature is not as clear as that between detection rate and extinction (see Fig.1.b). One of the causes may be the different column densities of the foreground gas. Different column densities of gas may cause different optical depths and then influence the absorption. Besides, when the gas density is not high enough, strong continuum emission can increase T_C and T_{ex} in Eq.2 simultaneously (see Appendix B). So a higher T_C may not necessarily increase the absorption even without the disturbance from column density. Complicated relations between T_L and T_C were also reported by Zhang et al. (2012) and Tang et al. (2014). Their results show that there is a certain correlation between T_L and T_C , but with considerable scatter.

4.2 H_2CO Absorption and $\text{H}_{110\alpha}$ Emission

Of all the 180 observed sources 36 have observed the $\text{H}_{110\alpha}$. In all the sources where $\text{H}_{110\alpha}$ were detected, five sources have no H_2CO , namely the following: IRAS00494+5617, IRAS03595+5110, IRAS05327-0529, IRAS06068+2030 and IRAS18151-1208. It may be caused by the lack of the foreground dense gas in front of the HII region. Figure.2 shows that most sources have a low absolute value ($-10 < V(\text{H}_2\text{CO}) - V(\text{H}_{110\alpha}) < 10 \text{ km s}^{-1}$) of two lines center velocity differences, which suggests that the H_2CO clouds associate well with the HII region and the relative motion between H_2CO clouds and HII region is quite small. This result agrees with the comparative results of H_2CO clouds and HII region by Downes et al. (1980) and Caswell and Haynes (1987). A few cases of H_2CO absorption components have large velocity differences with $\text{H}_{110\alpha}$ (above 20 km s^{-1}), which suggests that those H_2CO clouds could not be associated with a HII region. Similar results have been noted by Caswell and Haynes (1987), Pipenbrink and Wendker (1988), Du et al. (2011), and Han et al. (2011).

4.3 H_2CO Absorption and Infrared Emission

There are 152 IRAS sources in our observed sample. 110 H_2CO absorptions and 25 $\text{H}_{110\alpha}$ emissions were detected in all IRAS sources. A high detection ratio (about 72%) of H_2CO absorption shows that the excitation of the H_2CO absorption line may have some connection with the infrared emission. We compared

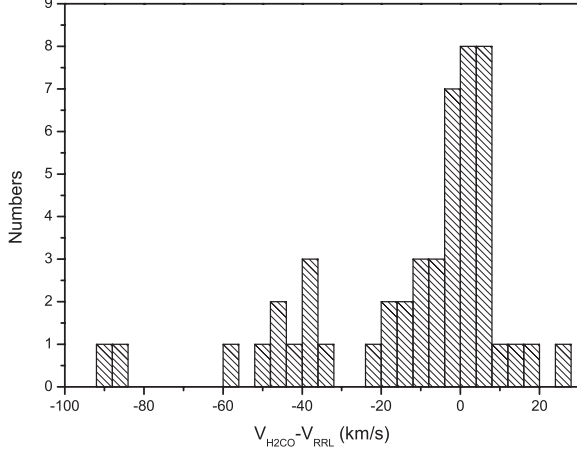


Fig. 2 Histogram of the line center velocity differences between H_2CO and $\text{H}_{110\alpha}$. All the velocity components of H_2CO are used.

the relation between the H_2CO flux density and IRAS flux density in the Fig.3. The sources were divided into two subsamples by the detection of RRLs. The fitting between $100\ \mu\text{m}$ and H_2CO flux density was made. The correlation factor of sources detected in RRLs is 0.47 and the correlation factor of sources not detected in RRLs is 0.24. This result shows that sources detected in RRLs have a certain correlation between $100\ \mu\text{m}$ and H_2CO flux density, while sources not detected in RRLs have no obvious correlation between $100\ \mu\text{m}$ and H_2CO flux density. This agrees with the result of Du et al. (2011). The $100\ \mu\text{m}$ flux densities of the sources not detected in RRLs have a lower value and a larger scatter. Without a HII region, the interstellar radiation field may contribute a lot in the $100\ \mu\text{m}$ flux of the sources not detected in RRLs and make the behaviors complex (Wu et al. 2005).

4.4 Comparison between H_2CO and NH_3

NH_3 is a high density tracer of $n[\text{H}_2] > 10^4\ \text{cm}^{-3}$ (Ungerechts et al. 1986), while the density of H_2CO absorption line is considered to be $10^3 < n[\text{H}_2] < 10^5\ \text{cm}^{-3}$ (Evans et al. 1975; Henkel et al. 1980). The lower density limit of H_2CO is little than that of NH_3 and nearly the same as the density at which ^{13}CO can probe ($\sim 10^3\ \text{cm}^{-3}$, Ungerechts et al. 1997; Wienen et al. 2012). So it would be inferred that the H_2CO roughly traces the region between that of ^{13}CO and NH_3 .

4.4.1 Line-center Velocity and Line Width

The correlation of NH_3 and ^{13}CO (1-0) emission towards $870\ \mu\text{m}$ sources was analyzed by Wienen et al.

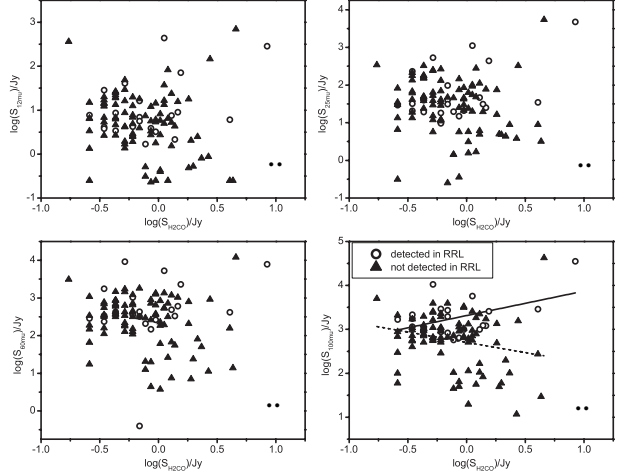


Fig. 3 Relationship between H_2CO flux density and infrared flux density of: a) $12\ \mu\text{m}$; b) $25\ \mu\text{m}$; c) $60\ \mu\text{m}$; d) $100\ \mu\text{m}$. The *cycles* are the sources detected in RRLs, and the *triangles* are sources not detected in RRLs. The *solid line* in d) is the fitting result of sources detected in RRLs, and the *dash line* is that of sources not detected in RRLs.

(2012). They observed NH_3 lines towards the APEX Telescope Large Area Survey (ATLASGAL) sources and extracted ^{13}CO (1-0) lines of the sources from the University-Five College Radio Astronomy Observatory Galactic Ring Survey (GRS) (Jackson et al. 2006). The line center velocity differences between ^{13}CO (1-0) and NH_3 lines are smaller than the NH_3 (1,1) line width for most of the sources. The line width of ^{13}CO is mostly broader than NH_3 lines. Turbulence or multiple structures within a large scale was considered to cause the ^{13}CO line width to be broader than that of NH_3 (Wienen et al. 2012).

We analyzed the line center velocities of NH_3 and H_2CO , and we found that 90% of the sources have a velocity difference $< 2.4\ \text{km s}^{-1}$ and 65% have a difference $< 1\ \text{km s}^{-1}$ (see Fig.4). This difference distribution is smaller than that between ^{12}CO and NH_3 shown in Churchwell et al. (1990), which they considered to be small enough to originate in the same dynamical system. Although more sources have negative velocity differences than positive values, this is of marginal significance given our velocity resolution. For most of the sources, the velocity difference is smaller than both the H_2CO line width and the NH_3 line width (see Fig.4). This behavior is similar to the results of the observations that searched for core-to-envelope relative motions (Walsh et al. 2007; Wienen et al. 2012).

Both H_2CO and NH_3 have HFS, so the observed line width cannot represent the Doppler width directly, as Nash (1990) suggested when they attempted to compare the line widths of these two lines. Usually, fitting to a less blended HFS component is used to get

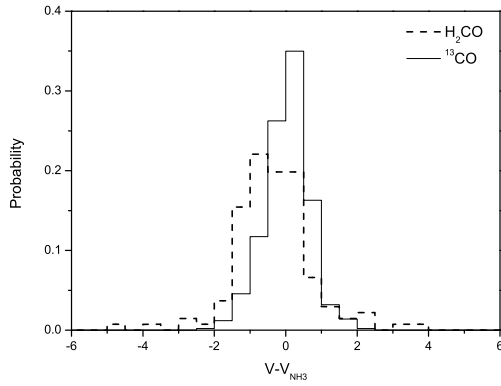


Fig. 4 The probability distribution of the V_{LSR} difference between molecules and NH_3 . The *dashed line* is the probability distribution of the velocity difference between our H_2CO observation and NH_3 ; the *solid line* is that between ^{13}CO and NH_3 from Wienen et al. (2012).

the intrinsic line width in this case, such as method $\text{NH}_3(1,1)$ fitting in CLASS software. But for $\text{H}_2\text{CO}(1_{10} - 1_{11})$ lines, the HSF components are too close together compared to the line width to make such a fitting. Even the farthest component from the group, $F=1-0$, is only about 1.2 km s^{-1} away from the group center, which can easily be blended in most sources, as is shown in Tucker et al. (1971). To solve this problem, we introduced a similar simulation following Barranco and Goodman (1998), to get a simulated intrinsic line width from direct observed value. The details of this simulation are presented in Appendix A, and the result shows that the difference between blended line width and intrinsic line width is less than 20% for most of our sources. So we did not distinguish between observed line width and intrinsic line width in the following discussions.

The mean value of H_2CO line width is 3.3 km s^{-1} , and that of $\text{NH}_3(1,1)$ lines is 1.9 km s^{-1} . On average, the line width of H_2CO is larger than that of $\text{NH}_3(1,1)$. We plotted the probability distribution of the line width ratio between H_2CO and NH_3 ($dV_{\text{H}_2\text{CO}}/dV_{\text{NH}_3}$) in Fig. 5. The distribution of the line width ratio between $^{13}\text{CO}(1-0)$ and $\text{NH}_3(1,1)$ ($dV_{^{13}\text{CO}}/dV_{\text{NH}_3}$) from Wienen et al. (2012) was also attached to Fig. 5. The curve shows that more than 88% of the sources have a H_2CO line width which is larger than NH_3 line width, and 80% of the sources have H_2CO line width which is 1.2 times larger than that of NH_3 . The distribution of $dV_{\text{H}_2\text{CO}}/dV_{\text{NH}_3}$ is very similar to that of $dV_{^{13}\text{CO}}/dV_{\text{NH}_3}$. The average of $dV_{^{13}\text{CO}}/dV_{\text{NH}_3}$ is 2.1 and that of $dV_{\text{H}_2\text{CO}}/dV_{\text{NH}_3}$ is 1.9. The max difference (D) of the two cumulative probability curve is

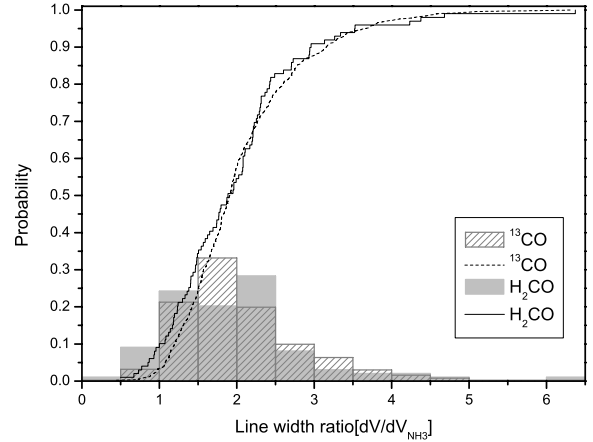


Fig. 5 The probability distribution of line width ratio between molecules and NH_3 , $dV_{^{13}\text{CO}}/dV_{\text{NH}_3}$ and $dV_{\text{H}_2\text{CO}}/dV_{\text{NH}_3}$. The *solid line* and *shaded histogram* are cumulative curve and probability distribution of the ratio between H_2CO and NH_3 ; the *dashed line* and the *gray histogram* are that between ^{13}CO and NH_3 from Wienen et al. (2012).

0.109. The Kolmogoroff-Smirnov (K-S) statistic probability (P value) of this D value is 0.265 with the parameter $N=82.72$, or $P=0.570$ with $N=50$. This similarity may indicate that the H_2CO line exist in the similar regions as the ^{13}CO does, which was considered to trace a larger scale than the NH_3 dose and to be broader than NH_3 line because of turbulence within that larger scale (Wienen et al. 2012). This also agrees with the spatial distribution relation between H_2CO and ^{13}CO observed in Tang et al. (2013).

4.4.2 Column Density and Abundance

The H_2CO and NH_3 column densities are plotted against the H_2 column density in Fig. 6. To match the regions observed by the molecules, we used the extinction data of the center ($1'$) for NH_3 and the average of extinction data within $10'$ for H_2CO . The correlation between $N[\text{H}_2\text{CO}]$ and $N[\text{H}_2]$ seems to be better than that between $N[\text{NH}_3]$ and $N[\text{H}_2]$. The Pearson correlation factor for data in Fig. 6.a) is 0.54 and that for Fig. 6.b) is -0.28. The extinctions are usually considered to be able to trace low H_2 density regions, even lower than ^{13}CO does (Goodman et al. 2009; Padoan et al. 2006). Then a better correlation between H_2CO and a low-density-sensitive tracer indicates that the H_2CO may also tend to trace the low density region. This agrees with the relative position of H_2CO and NH_3 got in Section 4.4.1 through the line width relation.

The abundance ratio of $X[\text{NH}_3]/X[\text{H}_2\text{CO}]$ was assumed to be the ratio of the column densities following Nash (1990). In the range of H_2 column density $N(\text{H}_2)$

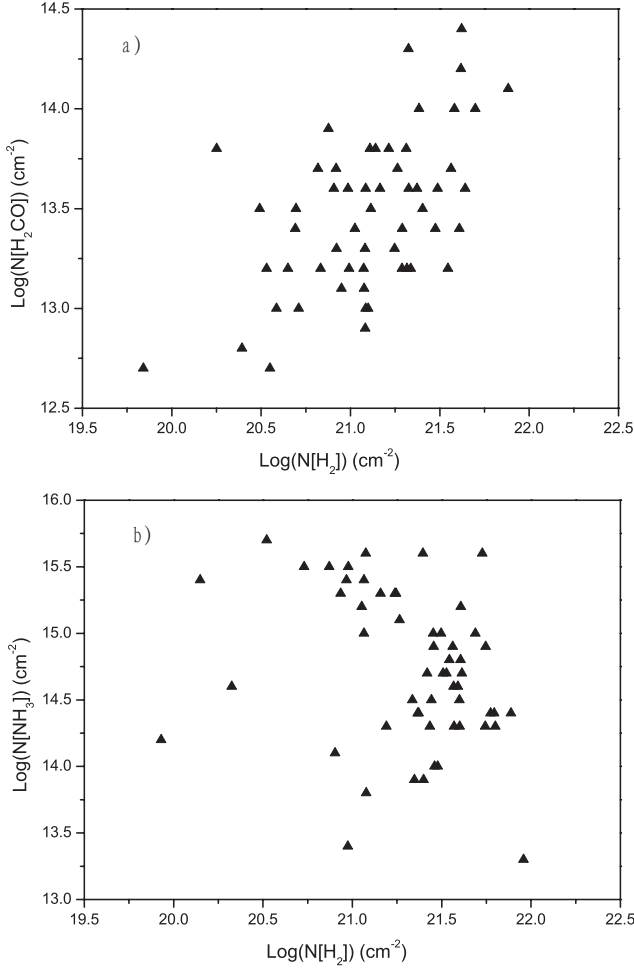


Fig. 6 H_2CO and NH_3 column density plotted against H_2 column density. The *upper panel* (a) is the column density of NH_3 and the *lower panel* (b) is that of H_2CO . The H_2 column density was calculated using $N(\text{H}_2) = 0.94 \times 10^{21} A_V \text{ (cm}^{-2}\text{)}$ in Bohlin et al. (1978).

$\sim 10^{19} - 10^{22} \text{ (cm}^{-2}\text{)}$, the majority of the abundance ratios $\log(X[\text{NH}_3]/X[\text{H}_2\text{CO}])$ have a range from 0 to 3 and the mean value of them is 1.26 (Fig.7). This mean value is approximately equal to the ratio predicted by models in Nash (1990), which gives an average value of 1.25 for $\log(X[\text{NH}_3]/X[\text{H}_2\text{CO}])$. But observations of Mebold et al. (1987) and Liszt et al. (2006) showed rather different values for the abundance ratio, -0.79 and -0.40 for $\log(X[\text{NH}_3]/X[\text{H}_2\text{CO}])$ respectively. Mebold et al. (1987) observed three high latitude clouds with these two molecules and Liszt et al. (2006) observed towards two local diffuse clouds, while Nash (1990) observed several sources in five clouds, and most of which have a latitude between $\pm 1^\circ$. According to McGehee (2008), most of the molecular clouds at high galactic latitude are proximity to the Sun. Then we may reach a hypothesis that the abundance ratios of NH_3 and H_2CO are different between local clouds

and other clouds. The sources of Mebold et al. (1987) and Liszt et al. (2006) are considered to be located in the local clouds and have a lower abundance ratio. We divided our sample into two subsamples by their galactic latitudes. The sources with $|b| > 5^\circ$ were assumed to be local clouds. The average value of the abundance ratio were calculated in each subsamples. The average abundance ratios of the two subsamples and the three literatures above are plotted in Fig.8 The sources suspected to be local clouds (inside the *gray box*) seem to have a lower $X[\text{NH}_3]/X[\text{H}_2\text{CO}]$ ratio than the others. This result suggests that there might be some differences in physical and chemical conditions between the two types of clouds.

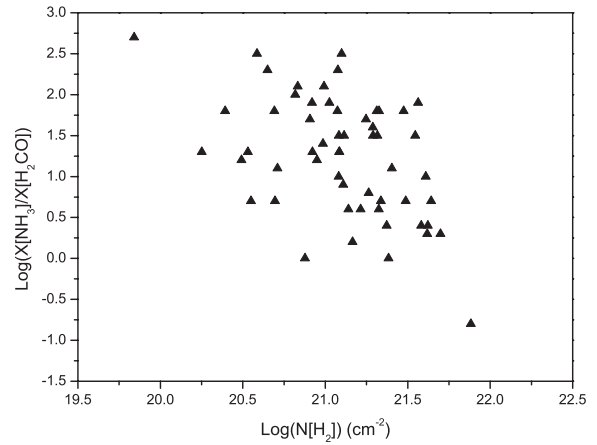


Fig. 7 Abundance ratio of NH_3 and H_2CO vs. H_2 column density.

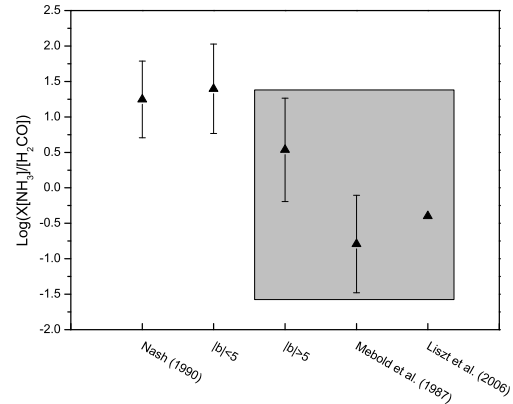


Fig. 8 The abundance ratio of NH_3 and H_2CO in local clouds and other clouds. The five columns of data points are the average of: models in Nash (1990); sources in our work that have galactic latitude smaller than 5° ; sources in our work that have galactic latitude larger than 5° ; data of Mebold et al. (1987); data of Liszt et al. (2006). The error bar is the standard deviation.

5 Summary

We observed 180 NH_3 sources and detected 138 sources with H_2CO ($1_{10} - 1_{11}$) lines and 36 with $\text{H}_{110\alpha}$ RRLs. Among the 138 H_2CO detections, 38 were considered as newly detected. The detection rate of H_2CO increases monotonically with the increasing of extinction, but it seems to have a complex relation with 6-cm continuum radiation. The line center velocity differences between H_2CO and NH_3 are small, which suggests that the two molecules should belong to the same dynamical system. The average line width of H_2CO is 2.1 times that of NH_3 , and the probability distribution curve of the line width ratios between H_2CO and NH_3 is close to that of ^{13}CO . This line width relation suggests that H_2CO may be distributed in a larger and lower density region than NH_3 does, and this is similar to that of ^{13}CO . The H_2CO column density correlated to H_2 column density (derived from extinction) well. This also suggests that the H_2CO exists in a larger scale than NH_3 . The Abundance ratio $X[\text{NH}_3]/X[\text{H}_2\text{CO}]$ varies from 1 to 10^3 and is significantly smaller in local clouds.

Acknowledgements We thank all the staff of Nanshan Observatory for observations. This work was funded by The National Natural Science foundation of China under grant 10778703 and partly supported by China Ministry of Science and Technology under State Key Development Program for Basic Research (2012CB821800) and the National Natural Science foundation of China under grant 11373062, 11303081 and 10873025.

References

- Barranco, J.A., Goodman, A.A.: *Astrophys. J.* **504**, 207 (1998)
- Bohlin, R.C., Savage, B.D., Drake, J.F.: *Astrophys. J.* **224**, 132 (1978)
- Caswell, J.L., Haynes, R.F.: *Astron. Astrophys.* **171**, 261 (1987)
- Churchwell, E., Walmsley, C.M., Cesaroni, R.: *Astron. Astrophys. Suppl. Ser.* **83**, 119 (1990)
- Darling, J., Zeiger, B.: *Astrophys. J. Lett.* **749**, 33 (2012)
- Dobashi, K.: *Publ. Astron. Soc. Jpn.* **63**, 1 (2011)
- Downes, D., Wilson, T.L., Bieging, J., Wink, J.: *Astron. Astrophys. Suppl. Ser.* **40**, 379 (1980)
- Du, Z.M., Zhou, J.J., Esimbek, J., Han, X.H., Zhang, C.P.: *Astron. Astrophys.* **532**, 127 (2011)
- Evans, N.J. II, Morris, G., Sato, T., Zuckerman, B.: *Astrophys. J.* **196**, 433 (1975)
- Garrison, B.J., Lester, W.A. Jr., Miller, W.H., Green, S.: *Astrophys. J. Lett.* **200**, 175 (1975)
- Goodman, A.A., Pineda, J.E., Schnee, S.L.: *Astrophys. J.* **692**, 91 (2009)
- Han, X.-H., Zhou, J.-J., Esimbek, J., Wu, G., Gao, M.-F.: *Research in Astronomy and Astrophysics* **11**, 156 (2011)
- Harju, J., Walmsley, C.M., Wouterloot, J.G.A.: *Astron. Astrophys. Suppl. Ser.* **98**, 51 (1993)
- Heiles, C.: *Astrophys. J.* **183**, 441 (1973)
- Henkel, C., Walmsley, C.M., Wilson, T.L.: *Astron. Astrophys.* **82**, 41 (1980)
- Ho, P.T.P., Townes, C.H.: *Annu. Rev. Astron. Astrophys.* **21**, 239 (1983)
- Jackson, J.M., Rathborne, J.M., Shah, R.Y., Simon, R., Bania, T.M., Clemens, D.P., Chambers, E.T., Johnson, A.M., Dormody, M., Lavoie, R., Heyer, M.H.: *Astrophys. J. Suppl. Ser.* **163**, 145 (2006)
- Kirk, H., Johnstone, D., Tafalla, M.: *Astrophys. J.* **668**, 1042 (2007)
- Liszt, H.S., Lucas, R., Pety, J.: *Astron. Astrophys.* **448**, 253 (2006)
- MacDonald, G.H., Little, L.T., Brown, A.T., Riley, P.W., Matheson, D.N., Felli, M.: *Mon. Not. R. Astron. Soc.* **195**, 387 (1981)
- Mangum, J.G., Wootten, A.: *Astrophys. J. Suppl. Ser.* **89**, 123 (1993)
- Mangum, J.G., Darling, J., Menten, K.M., Henkel, C.: *Astrophys. J.* **673**, 832 (2008)
- Mangum, J.G., Darling, J., Henkel, C., Menten, K.M.: *Astrophys. J.* **766**, 108 (2013)
- McGehee, P.M.: In: Reipurth, B. (ed.) *Star Formation and Molecular Clouds at High Galactic Latitude*, p. 813 (2008)
- Mebold, U., Heithausen, A., Reif, K.: *Astron. Astrophys.* **180**, 213 (1987)
- Myers, P.C., Benson, P.J.: *Astrophys. J.* **266**, 309 (1983)
- Nash, A.G.: *Astrophys. J. Suppl. Ser.* **72**, 303 (1990)
- Padoan, P., Cambr  sy, L., Juvela, M., Kritsuk, A., Langer, W.D., Norman, M.L.: *Astrophys. J.* **649**, 807 (2006)
- Pipenbrink, A., Wendker, H.J.: *Astron. Astrophys.* **191**, 313 (1988)
- Ridge, N.A., Di Francesco, J., Kirk, H., Li, D., Goodman, A.A., Alves, J.F., Arce, H.G., Borkin, M.A., Caselli, P., Foster, J.B., Heyer, M.H., Johnstone, D., Kosslyn, D.A., Lombardi, M., Pineda, J.E., Schnee, S.L., Tafalla, M.: *Astron. J.* **131**, 2921 (2006)
- Scalise, E. Jr., Schaal, R.E., Bakor, Y., Vilas Boas, J.W.S., Myers, P.C.: *Astron. J.* **86**, 1939 (1981)
- Schreyer, K., Henning, T., Koempe, C., Harjunp  ae, P.: *Astron. Astrophys.* **306**, 267 (1996)
- Snyder, L.E., Buhl, D., Zuckerman, B., Palmer, P.: *Physical Review Letters* **22**, 679 (1969)
- Sridharan, T.K., Beuther, H., Schilke, P., Menten, K.M., Wyrowski, F.: *Astrophys. J.* **566**, 931 (2002)
- Sun, X.H., Han, J.L., Reich, W., Reich, P., Shi, W.B., Wielebinski, R., F  rst, E.: *Astron. Astrophys.* **463**, 993 (2007)
- Tang, X.D., Esimbek, J., Zhou, J.J., Wu, G., Ji, W.G., Okoh, D.: *Astron. Astrophys.* **551**, 28 (2013)
- Tang, X.D., Esimbek, J., Zhou, J.J., Wu, G., Okoh, D.: *ArXiv1402.5471* (2014)
- Townes, C.H., Cheung, A.C.: *Astrophys. J. Lett.* **157**, 103 (1969)
- Tucker, K.D., Tomasevich, G.R., Thaddeus, P.: *Astrophys. J.* **169**, 429 (1971)
- Ungerechts, H., Winnewisser, G., Walmsley, C.M.: *Astron. Astrophys.* **157**, 207 (1986)
- Ungerechts, H., Bergin, E.A., Goldsmith, P.F., Irvine, W.M., Schloerb, F.P., Snell, R.L.: *Astrophys. J.* **482**, 245 (1997)
- van der Tak, F.F.S., Black, J.H., Sch  ier, F.L., Jansen, D.J., van Dishoeck, E.F.: *Astron. Astrophys.* **468**, 627 (2007)
- Vanden Bout, P.A., Snell, R.L., Wilson, T.L.: *Astron. Astrophys.* **118**, 337 (1983)
- Walmsley, C.M., Ungerechts, H.: *Astron. Astrophys.* **122**, 164 (1983)
- Walsh, A.J., Myers, P.C., Di Francesco, J., Mohanty, S., Bourke, T.L., Gutermuth, R., Wilner, D.: *Astrophys. J.* **655**, 958 (2007)
- Wienen, M., Wyrowski, F., Schuller, F., Menten, K.M., Walmsley, C.M., Bronfman, L., Motte, F.: *Astron. Astrophys.* **544**, 146 (2012)
- Wu, J., Evans, N.J. II, Gao, Y., Solomon, P.M., Shirley, Y.L., Vanden Bout, P.A.: *Astrophys. J. Lett.* **635**, 173 (2005)
- Young, K.E., Lee, J.-E., Evans, N.J. II, Goldsmith, P.F., Doty, S.D.: *Astrophys. J.* **614**, 252 (2004)
- Zhang, C.P., Esimbek, J., Zhou, J.J., Wu, G., Du, Z.M.: *Astrophys. Space Sci.* **337**, 283 (2012)

A Simulation of Blended H₂CO HFS

The optical depth of all the HFS is simply assumed to be a superposition of N components,

$$\tau(v) = \sum_{j=1}^N \alpha_j \tau_0 \exp\left\{-4 \ln 2 \left[\frac{v - (v_j + v_0)}{\Delta v_{int}}\right]^2\right\} \quad (A1)$$

where α_j and v_j are the intensity and velocity of the j th HFS component, and Δv_{int} is the intrinsic line width. The α_j and v_j data of H₂CO(1₁₀ – 1₁₁) HFS components were got from (Tucker et al. 1971). Because the optical depth of H₂CO(1₁₀ – 1₁₁) in most cases is far less than 1, we assume that the intensity is proportional to the opacity. So the spectra line profile is the same as $\tau(v)$.

Spectra for Δv_{int} between 0.43 to 8.69 at intervals of 0.43 km/s (7 KHz to 140 KHz at intervals of 7 KHz) were calculated using Eq.A1. Then single gaussian fittings were made to get the blended line width. The simulated spectra are shown in Fig.14 and the fitting results are listed in Table. 1. The ratios between blended and unblended line widths are plotted in Fig.9. Because most of our observed line widths are larger than 1 km s^{-1} , this HFS blending effect would not make much difference as regards our sources.

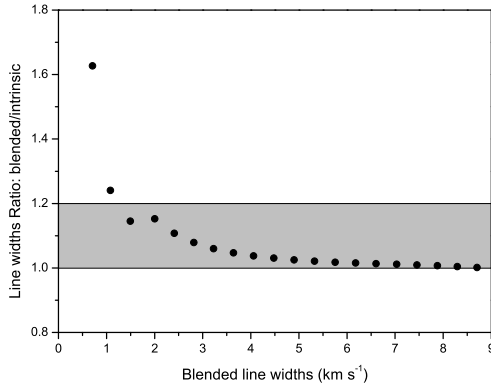


Fig. 9 The ratio of blended line width to intrinsic line width is plotted against the blended line width. The *gray box* is the region with a ratio between 1.2 and 1.

B Non-LTE Radiative Transfer of H₂CO

To absorb the CMB radiation as observed, the H₂CO 1₁₀ – 1₁₁ transition must have an excitation temperature lower than CMB. The different cross sections of transitions in collision are considered to be the most likely reason to generate such a low excitation temperature (Townes and Cheung 1969; Garrison et al.

Table 1 HFS simulation result

Intrinsic linewidth (km s^{-1})	Observed linewidth (km s^{-1})
0.43	0.71
0.87	1.08
1.30	1.49
1.74	2.00
2.17	2.41
2.61	2.81
3.04	3.22
3.48	3.64
3.91	4.06
4.35	4.48
4.78	4.90
5.21	5.32
5.65	5.75
6.08	6.18
6.52	6.60
6.95	7.03
7.39	7.45
7.82	7.88
8.26	8.29
8.69	8.70

1975; Evans et al. 1975). The excitation of H₂CO should be treated with a non-LTE method, because the LTE approximation would cause an excitation temperature above CMB. We used the Radex Non-LTE molecular radiative transfer code (van der Tak et al. 2007) to calculate the excitation of H₂CO. The predicted line brightness temperature (T_L) and excitation temperature (T_{ex}) were calculated from the input H₂ number density ($n[\text{H}_2]$), H₂CO column density ($N[\text{H}_2\text{CO}]$), background brightness temperature (T_{bg}) and kinetic temperature (T_{kin}), where T_{bg} is the background brightness temperature, which is equal to $T_C + T_{CMB}$ in Eq.2.

The result shows that the competition between collision and background radiation dominates the excitation process of H₂CO. Figure.10 shows T_{ex} vs. T_{bg} under different T_{kin} and $n[\text{H}_2]$. Under both low $n[\text{H}_2]$ and high $n[\text{H}_2]$ conditions, T_{ex} is less sensitive to T_{kin} at high T_{kin} ($T_{kin} > 20\text{K}$). A similar relation between T_{ex} and T_{kin} was obtained by Darling and Zeiger (2012) in high redshift galaxies. At low $n[\text{H}_2]$, collisions are insufficient. Then the background radiation dominates the level populations and the excitation temperature of H₂CO almost follows the variation of T_{bg} , i.e. $T_{ex} \approx T_{bg} - \text{Constant}$, as is shown in Fig.10.a). This may contribute to the less clear relation between the detection rate and T_C in Fig.1.b). At high $n[\text{H}_2]$, collisions dominate the level populations and the excitation temperature keeps almost constant over the whole T_{bg} range.

The possible $n[\text{H}_2]$ values of H_2CO 6-cm lines are considered to be $10^3 < n[\text{H}_2] < 10^5 (\text{cm}^{-3})$ (Evans et al. 1975; Henkel et al. 1980). The exact value of $n[\text{H}_2]$, which in principle can be derived through the relative intensity of $1_{10} - 1_{11}$ (6 cm) and $2_{11} - 2_{12}$ (2 cm) (Henkel et al. 1980; Mangum et al. 2008), is unknown because only the 6-cm lines were observed. But in that $n[\text{H}_2]$ interval, the $n[\text{H}_2]$ seems not to influence the $N[\text{H}_2\text{CO}]$ too much, as the contours in that region in Fig.11.a) are almost parallel to the horizontal axis. To find the potential uncertainty introduced by the unknown $n[\text{H}_2]$, we calculated the $N[\text{H}_2\text{CO}]$ under the assumptions that $n[\text{H}_2]=10^2, 10^3, 10^4$, and $10^5 (\text{cm}^{-3})$ respectively. The histogram distributions of the column densities are plotted in Fig. 11.b). The column density distributions of $n[\text{H}_2]=10^3, 10^4$, and $10^5 (\text{cm}^{-3})$ are almost the same, and that of $n[\text{H}_2]=10^2 (\text{cm}^{-3})$ is about one order larger than the others. We also plotted the histogram distribution of column densities under the assumption that $T_{\text{ex}}=1.7\text{K}$ in Section 3. The $N[\text{H}_2\text{CO}]$ distribution of $T_{\text{ex}}=1.7\text{K}$ is about half an order larger than that of $10^3 < n[\text{H}_2] < 10^5 (\text{cm}^{-3})$.

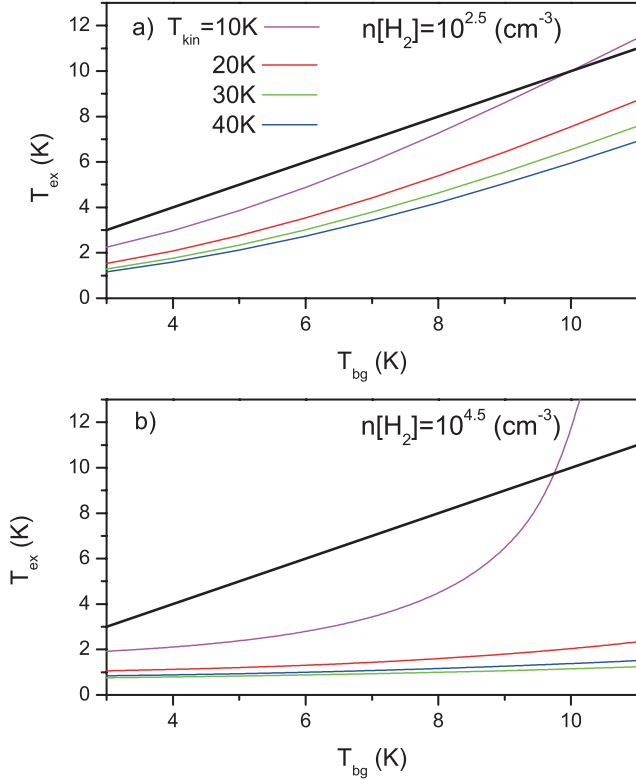


Fig. 10 Excitation temperature of H_2CO vs. background brightness temperature. The *thick black line* is for $T_{\text{ex}} = T_{\text{bg}}$.

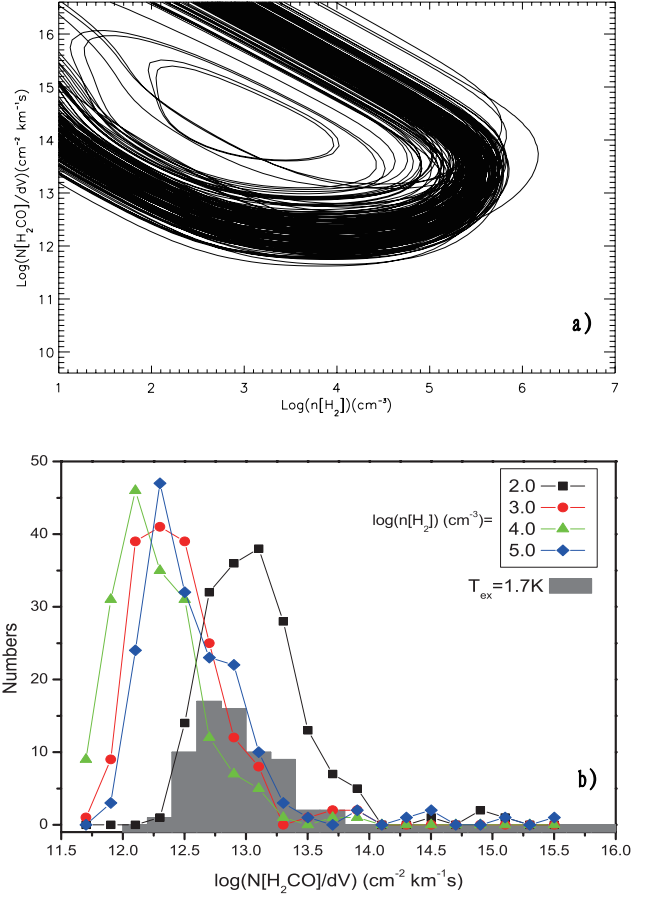


Fig. 11 a), Contours of T_L in $\log(n[\text{H}_2]) - \log(N[\text{H}_2\text{CO}])$ space. The figure presented a map of calculated T_L in $\log(n[\text{H}_2]) - \log(N[\text{H}_2\text{CO}])$ space. For each source, one contour on which T_L is equal to the observed T_{MB} is drawn. b) Histogram of $N[\text{H}_2\text{CO}]$ under different assumptions: $n[\text{H}_2]=10^2, 10^3, 10^4, 10^5 (\text{cm}^{-3})$ and $T_{\text{ex}}=1.7\text{K}$.

Table 2 Source

Number	Source	RA (J2000) h:m:s	Dec (J2000) °:':"	A_v (mag)	T_C (K)	$V_{LSR(1,1)}$ ($km\ s^{-1}$)	$\Delta V_{(1,1)}$ ($km\ s^{-1}$)	$N[NH_3]$ ($10^{13} cm^{-2}$)	H110 $_{\alpha}$ ^a Detected?	H ₂ CO ^b Detected?	ref ^c
001	IRAS00338+6312	00:36:47.5	+63:29:02	1.03	...	-17.8	2.3	99.8	0	1	3
002	IRAS00494+5617	00:52:23.7	+56:33:45	0.87	0.67	-30.3	2.6	87.0	1	0	2
003	IRAS01194+6136	01:22:48.6	+61:52:15	4.76	0.16	0	1	3
004	IRAS02219+6152	02:25:42.8	+62:06:05	3.20	8.84	0	1	3
005	IRAS02230+6202	02:26:50.8	+62:15:52	1.49	3.70	1	1	3
006	IRAS02232+6138	02:27:01.1	+61:52:14	2.20	1.20	-46.5	2.7	51.4	1	1	3
007	IRAS02244+6117	02:28:14.0	+61:31:12	1.33	0.91	-49.7	2.1	...	1	1	3
008	IRAS02575+6017	03:01:32.3	+60:29:12	1.29	0.22	-38.1	2.0	24.7	0	1	3
009	IRAS02593+6016	03:03:17.9	+60:27:52	1.15	0.17	-38.3	1.8	...	0	1	3
010	IRAS03035+5819	03:07:25.6	+58:30:52	0.41	0.02	-39.6	1.7	11.7	0	0	3
011	IRAS03064+5638	03:10:15.3	+56:50:18	0.47	0.03	0	0	3
012	IRAS03211+5446	03:24:59.1	+54:57:25	0.66	0.03	0	0	3
013	IRAS03236+5836	03:27:38.6	+58:46:58	3.86	...	-12.9	2.3	...	0	1	3
014	GGD2-3	03:28:50.3	+31:06:19	2.31	...	7.2	1.1	...	0	2	1
015	IRAS03260+3111	03:29:10.4	+31:21:59	4.76	0	1	3
016	IRAS03595+5110	04:03:17.7	+51:18:57	0.06	1.52	1	0	3
017	IRAS04073+5102	04:11:05.6	+51:10:16	0.37	1.57	1	2	3
018	IRAS04269+3510	04:30:14.4	+35:16:30	4.63	0.03	0	2	3
019	IRAS04324+5106	04:36:19.7	+51:12:45	1.28	0.04	-36.0	3.2	...	0	2	3
020	IRAS04329+5047	04:36:48.5	+50:53:25	0.46	0.10	0	2	3
021	IRAS05100+3723	05:13:25.4	+37:27:04	0.41	0.15	0	2	3
022	IRAS05197+3355	05:23:04.5	+33:58:27	0.09	0.15	0	0	3
023	IRAS05274+3345	05:30:45.6	+33:47:52	0.33	...	-3.6	2.2	45.9	0	2	3
024	IRAS05281+3412	05:31:26.6	+34:14:58	0.92	0.12	0	0	3
025	IRAS05302-0537	05:32:41.7	-05:35:48	1.75	...	8.8	0.7	48.0	0	2	2
026	IRAS05327-0529	05:35:10.0	-05:27:53	1.85	25.55	9.2	1.5	58.0	1	0	2
027	IRAS05327-0457	05:35:14.4	-04:55:45	3.53	...	11.9	1.5	...	0	1	3
028	IRAS05334-0611	05:35:51.9	-06:10:00	1.09	...	8.6	1.3	26.0	0	2	2
029	IRAS05338-0624	05:36:19.0	-06:22:13	2.07	...	7.1	1.0	166.0	0	1	2
030	IRAS05340-0603	05:36:28.2	-06:01:18	0.30	0.03	8.2	0.6	81.0	0	2	2
031	IRAS05341-0530	05:36:38.4	-05:28:16	0.87	0.29	0	0	3
032	IRAS05345+3157	05:37:47.8	+31:59:24	1.01	0	2	3
033	IRAS05363-0702	05:38:46.4	-07:01:05	6.63	...	3.3	0.9	22.0	0	2	2
034	IRAS05355+3039	05:38:47.2	+30:41:28	1.51	0.01	0	0	3
035	IRAS05358+3543	05:39:10.4	+35:45:19	1.28	0.03	-17.4	2.2	50.9	0	1	3
036	IRAS05375-0731	05:39:56.1	-07:30:26	5.50	...	4.8	1.1	98.0	0	1	2
037	IRAS05378-0750	05:40:16.7	-07:48:33	4.42	...	4.6	0.4	33.0	0	2	2
038	GGD4	05:40:25.1	+23:50:56	1.47	...	2.3	1.9	24.7	0	1	1
039	S235	05:40:51.5	+35:41:31	3.55	0.07	-17.0	2.0	...	0	2	1
040	GGD7	05:40:48.2	-08:07:31	5.31	0.01	5.6	1.3	18.8	0	1	1
041	IRAS05387-0149	05:41:19.0	-01:47:33	6.99	0.90	10.3	1.6	...	1	1	3
042	IRAS05389-0756	05:41:23.8	-07:55:13	4.45	0.05	4.5	0.7	62.0	0	1	2
043	IRAS05391-0217	05:41:37.9	-02:15:52	4.21	0	1	3
044	IRAS05393-0156	05:41:49.5	-01:55:17	8.73	7.72	10.7	2.1	(2.2)	1	1	3
045	IRAS05403-0818	05:42:47.3	-08:17:06	2.28	0.40	3.3	0.8	51.0	0	0	2
046	IRAS05404-0948	05:42:47.7	-09:47:24	4.33	0.05	2.9	0.5	25.0	0	2	2
047	IRAS05405-0117	05:43:02.5	-01:16:23	4.93	...	9.3	0.3	119.0	0	1	2
048	IRAS05413-0104	05:43:51.5	-01:02:52	0.26	0.04	1.7	0.6	37.0	0	2	2
049	IRAS05435-0015	05:46:04.5	-00:14:22	3.59	0.01	10.4	0.6	67.0	0	0	2

Table 2—Continued

Number	Source	RA(J2000) h:m:s	Dec(J2000) °:′:″	A_v (mag)	T_C (K)	$V_{LSR(1,1)}$ ($km\ s^{-1}$)	$\Delta V_{(1,1)}$ ($km\ s^{-1}$)	$N[NH_3]$ ($10^{13} cm^{-2}$)	H110 $_{\alpha}$ ^a Detected?	H ₂ CO ^b Detected?	ref ^c
050	IRAS05437-0001	05:46:17.8	-00:00:17	5.16	0	1	3
051	IRAS05450+0019	05:47:34.6	+00:20:08	6.85	...	9.2	0.8	60.0	0	1	2
052	IRAS05480+2545	05:51:10.8	+25:46:14	1.30	0.01	-9.4	2.3	79.7	0	2	3
053	IRAS05490+2658	05:52:12.9	+26:59:33	1.96	0.05	0.8	1.5	22.7	0	1	3
054	IRAS05553+1631	05:58:13.9	+16:32:00	0.92	...	5.7	2.2	...	0	0	3
055	IRAS06006+3015	06:03:54.1	+30:14:55	0.20	0.05	-8.7	1.6	(3.2)	0	1	3
056	IRAS06013+3030	06:04:34.3	+30:30:40	1.92	0.01	0	0	3
057	MON-R2	06:07:45.3	-06:23:09	5.16	...	10.3	2.6	10.8	1	1	1
058	IRAS06055+2039	06:08:32.8	+20:39:16	1.42	0.18	8.7	2.8	48.3	0	1	3
059	IRAS06056+2131	06:08:41.0	+21:31:01	1.30	0.07	2.6	1.6	19.4	0	1	3
060	IRAS06061+2151	06:09:07.8	+21:50:39	1.37	0.01	-0.6	3.1	56.1	0	2	3
061	IRAS06063+2040	06:09:21.9	+20:39:28	1.34	0.65	0	0	3
062	IRAS06068+2030	06:09:51.7	+20:30:04	0.81	0.88	1	0	3
063	IRAS06073+1249	06:10:12.4	+12:48:46	0.17	0.02	0	0	3
064	GGD12-15	06:10:54.5	-06:11:28	2.53	...	11.7	1.4	6.1	0	1	1
065	GGD16-17	06:12:47.5	-06:13:51	1.64	0.15	11.7	1.9	...	0	2	1
066	IRAS06105+1756	06:13:28.3	+17:55:30	1.52	0.08	0	2	3
067	IRAS06114+1745	06:14:23.7	+17:44:36	0.66	0.01	8.1	1.9	...	0	2	3
068	IRAS06117+1350	06:14:36.6	+13:49:35	0.22	0.08	0	2	3
069	IRAS06155+2319	06:18:35.2	+23:18:11	1.59	0.07	0	0	3
070	IRAS06308+0402	06:33:31.1	+04:00:07	1.87	0.04	0	2	3
071	ROSETTE-IRS	06:34:35.6	+04:12:38	2.75	0.08	12.6	1.3	...	0	2	1
072	IRAS06380+0949	06:40:45.7	+09:46:33	1.73	0.09	0	1	3
073	IRAS06384+0932	06:41:11.0	+09:29:32	2.25	0.07	7.9	2.6	80.6	0	1	3
074	IRAS06412-0105	06:43:45.0	-01:08:07	0.02	0.07	0	0	3
075	IRAS06567-0355	06:59:15.8	-03:59:39	0.89	0.02	25.0	2.2	39.3	0	2	3
076	IRAS06581-0848	07:00:30.9	-08:52:40	0.29	0.01	0	1	3
077	IRAS07029-1215	07:05:16.9	-12:20:02	1.02	0.14	0	0	3
078	IRAS07061-0414	07:08:38.8	-04:19:08	0.04	0.08	0	0	3
079	IRAS07299-1651	07:32:10.0	-16:58:15	1.43	0.08	0	0	3
080	IRAS07427-2400	07:44:51.9	-24:07:41	0.03	0.01	0	0	3
081	IRAS18090-1832	18:12:01.9	-18:31:56	-0.09	0.94	109.8	3.0	457.1	0	1	4
082	IRAS18102-1800	18:13:12.2	-17:59:35	0.48	1.67	21.1	2.2	295.1	1	1	4
083	IRAS18089-1732	18:11:51.3	-17:31:29	3.89	0.53	33.8	3.5	416.9	0	1	4
084	IRAS18159-1550	18:18:47.3	-15:48:58	1.02	0.82	59.9	0	1	4
085	IRAS18151-1208	18:17:57.1	-12:07:22	0.46	1.34	32.8	1	0	4
086	IRAS18182-1433	18:21:07.9	-14:31:53	1.05	0.78	59.1	3.0	213.8	0	1	4
087	IRAS18223-1243	18:25:10.9	-12:42:17	1.13	0.99	45.5	1.7	218.8	0	1	4
088	IRAS18272-1217	18:30:02.7	-12:15:27	0.35	0.42	34.0	0	0	4
089	IRAS18264-1152	18:29:14.3	-11:50:26	3.18	0.59	43.6	2.4	166.0	0	1	4
090	IRAS18247-1147	18:27:31.1	-11:45:56	0.17	0.95	121.7	3.3	151.4	0	0	4
091	IRAS18290-0924	18:31:44.8	-09:22:09	0.07	1.02	84.3	1.7	302.0	1	1	4
092	IRAS18308-0841	18:33:31.9	-08:39:17	0.63	1.07	77.1	1.9	354.8	0	1	4
093	IRAS18310-0825	18:33:47.2	-08:23:35	0.70	1.78	84.4	2.7	467.7	1	1	4
094	G23.95+0.15	18:34:24.0	-07:54:53	0.53	1.19	80.6	2.1	16.4	0	1	1
095	IRAS18337-0743	18:36:29.0	-07:40:33	2.18	1.82	57.9	2.6	426.6	1	1	4
096	G24.49-0.04	18:36:05.5	-07:31:23	2.32	1.71	109.6	2.6	8.4	1	1	1
097	G24.8+0.1	18:36:12.2	-07:11:55	2.10	2.42	110.2	3.2	...	0	1	1
098	IRAS18345-0641	18:37:16.8	-06:38:32	0.51	1.27	95.9	0	0	4

Table 2—Continued

Number	Source	RA(J2000) h:m:s	Dec(J2000) °:′:″	A_v (mag)	T_C (K)	$V_{LSR(1,1)}$ ($km\ s^{-1}$)	$\Delta V_{(1,1)}$ ($km\ s^{-1}$)	$N[NH_3]$ ($10^{13} cm^{-2}$)	H110 $_{\alpha}$ ^a Detected?	H ₂ CO ^b Detected?	ref ^c
099	IRAS18348-0616	18:37:29.0	-06:14:15	0.25	2.19	109.5	1.8	245.5	1	1	4
100	IRAS18372-0541	18:39:56.0	-05:38:49	0.56	1.36	23.6	1.5	61.7	0	1	4
101	IRAS18385-0512	18:41:12.0	-05:09:06	0.26	1.41	26.0	2.8	120.2	0	0	4
102	G28.86+0.07	18:43:45.9	-03:35:36	0.39	1.28	99.8	1.9	...	0	1	1
103	IRAS18431-0312	18:45:46.9	-03:09:24	0.59	0.86	105.2	1.4	239.9	0	0	4
104	IRAS18460-0307	18:48:39.2	-03:03:53	0.86	0.55	83.7	2.2	213.8	0	2	4
105	W43S	18:46:03.9	-02:39:12	0.79	3.14	97.6	3.2	...	1	1	1
106	IRAS18447-0229	18:47:23.7	-02:25:55	1.27	2.32	102.6	1.8	229.1	1	1	4
107	IRAS18437-0216	18:46:22.7	-02:13:24	0.52	1.49	110.8	1.8	166.0	1	2	4
108	IRAS18426-0204	18:45:12.8	-02:01:12	0.72	0.77	15.0	2.1	195.0	0	1	4
109	IRAS18454-0158	18:48:01.3	-01:54:49	0.74	4.18	52.6	1.7	147.9	1	1	4
110	IRAS18440-0148	18:46:36.3	-01:45:23	0.89	1.65	97.6	1.9	389.0	1	1	4
111	IRAS18454-0136	18:48:03.7	-01:33:23	1.26	1.99	38.9	2.5	100.0	0	1	4
112	G31.4-0.3	18:47:34.2	-01:12:46	0.91	0.80	96.2	2.3	...	0	1	1
113	IRAS18488+0000	18:51:24.8	+00:04:19	0.07	0.93	82.7	2.4	251.2	1	1	4
114	IRAS18472-0022	18:49:50.7	-00:19:09	-0.02	0.52	49.0	2.0	147.9	0	0	4
115	IRAS18470-0044	18:49:36.7	-00:41:05	0.12	0.83	96.5	3.9	501.2	0	0	4
116	IRAS18502+0051	18:52:50.3	+00:55:29	1.64	0.74	107.5	2.0	162.0	0	1	2
117	W48	19:01:47.5	+01:13:12	1.74	2.54	42.6	1.9	25.0	1	1	1
118	S68	18:30:00.4	+01:14:05	5.57	...	7.8	1.8	6.5	0	2	1
119	G34.3+0.1	18:53:18.4	+01:14:46	2.58	2.43	58.1	2.8	9.2	1	1	1
120	IRAS18521+0134	18:54:40.8	+01:38:02	1.24	1.09	76.0	2.0	169.8	0	0	4
121	IRAS18515+0157	18:54:04.2	+02:01:34	3.27	0.62	52.9	1.9	22.0	0	1	2
122	IRAS18530+0215	18:55:34.2	+02:19:08	2.25	1.03	77.7	3.7	263.0	0	1	4
123	IRAS18540+0220	18:56:35.6	+02:24:54	-0.07	1.24	49.6	3.9	27.5	1	1	4
124	IRAS18566+0408	18:59:09.9	+04:12:14	1.77	1.04	85.2	0	1	4
125	IRAS18553+0414	18:57:52.9	+04:18:06	1.34	0.55	10.0	3.0	316.2	0	1	4
126	IRAS18517+0437	18:54:13.8	+04:41:32	1.17	0.28	43.9	0	0	4
127	IRAS19012+0536	19:03:45.1	+05:40:40	0.70	0.63	65.8	2.6	15.5	0	0	4
128	IRAS19035+0641	19:06:01.1	+06:46:35	0.33	0.32	32.4	0	0	4
129	S76E	18:56:11.8	+07:53:24	3.22	0.85	32.7	2.3	...	1	1	1
130	IRAS19074+0752	19:09:53.3	+07:57:22	0.74	0.34	54.8	0	1	4
131	G45.49+0.13	19:14:11.2	+11:13:01	0.08	1.29	59.3	1.9	...	1	1	1
132	IRAS19175+1357	19:19:49.1	+14:02:46	0.26	0.91	14.6	1	1	4
133	IRAS19220+1432	19:24:19.7	+14:38:03	0.24	0.75	68.8	1	1	4
134	IRAS19217+1651	19:23:58.8	+16:57:37	-0.01	0.28	3.5	2.8	239.9	0	1	4
135	IRAS19266+1745	19:28:54.0	+17:51:56	3.73	0.38	5.0	2.5	53.7	0	1	4
136	IRAS19282+1814	19:30:28.1	+18:20:53	2.07	0.38	23.6	1.0	57.5	0	1	4
137	IRAS19403+2258	19:42:27.2	+23:05:12	0.74	0.22	26.7	1.0	...	0	0	4
138	IRAS19411+2306	19:43:18.1	+23:13:59	1.88	0.45	29.0	1.6	97.7	0	1	4
139	IRAS19413+2332	19:43:28.9	+23:40:04	1.89	0.17	20.8	0	1	4
140	S87	19:46:20.5	+24:35:22	0.38	0.26	24.1	1.7	2.7	0	1	1
141	S88	19:46:49.7	+25:12:56	1.57	0.84	21.8	2.1	...	1	1	1
142	IRAS19471+2641	19:49:09.9	+26:48:52	0.48	0.62	21.0	1	1	4
143	IRAS20081+2720	20:10:11.5	+27:29:06	4.21	...	5.7	0	1	4
144	ON1	20:10:09.2	+31:31:36	0.80	0.03	11.0	2.5	7.9	0	1	1
145	IRAS20051+3435	20:07:03.8	+34:44:35	0.31	0.11	11.6	0	1	4
146	S106	20:27:19.9	+37:22:42	1.90	1.84	-1.5	1.7	15.5	0	1	1
147	ON2	20:21:42.1	+37:26:08	0.64	1.40	-0.3	3.0	...	1	1	1

Table 2—Continued

Number	Source	RA(J2000) h:m:s	Dec(J2000) °:′:″	A_v (mag)	T_C (K)	$V_{LSR(1,1)}$ ($km\ s^{-1}$)	$\Delta V_{(1,1)}$ ($km\ s^{-1}$)	$N[NH_3]$ ($10^{13} cm^{-2}$)	H110 $_{\alpha}$ ^a Detected?	H ₂ CO ^b Detected?	ref ^c
148	IRAS20205+3948	20:22:21.9	+39:58:05	2.40	1.55	-1.7	0	1	4
149	IRAS20293+3952	20:31:10.7	+40:03:10	2.49	0.80	6.3	0	2	4
150	IRAS20275+4001	20:29:24.1	+40:11:14	0.35	1.16	-5.3	2.4	15.0	1	1	2
151	IRAS20126+4104	20:14:26.0	+41:13:32	0.02	0.45	-3.8	0	0	4
152	IRAS20216+4107	20:23:23.8	+41:17:40	2.54	1.00	-2.0	0	2	4
153	R131	20:24:25.7	+42:16:05	1.56	0.65	5.0	1.7	7.1	0	1	1
154	IRAS20319+3958	20:33:49.3	+40:08:45	0.30	0.51	8.8	0	1	4
155	IRAS20332+4124	20:35:00.5	+41:34:48	0.20	1.26	-2.0	0	0	4
156	IRAS20343+4129	20:36:07.1	+41:40:01	0.74	1.49	11.5	0	1	4
157	IRAS22308+5812	22:32:46.0	+58:28:22	0.07	0.13	-51.8	2.3	24.0	0	1	2
158	IRAS22444+5827	22:46:27.3	+58:43:18	1.28	0.04	-3.1	0.7	18.0	0	1	2
159	IRAS22134+5834	22:15:09.1	+58:49:09	0.86	0.06	-18.3	0	2	4
160	IRAS22267+6244	22:28:29.3	+62:59:44	1.38	0.04	-1.7	1.3	108.0	0	2	2
161	S140	22:19:22.2	+63:19:05	2.51	0.08	-7.1	1.8	10.2	0	2	1
162	R146	21:43:49.5	+66:06:46	1.31	...	-9.8	0.9	4.9	0	1	1
163	IRAS22539+5758	22:56:00.0	+58:14:46	0.36	0.05	-53.6	0.9	33.0	0	2	2
164	IRAS22566+5830	22:58:41.3	+58:46:57	0.19	0.24	-50.6	1.8	133.0	0	2	2
165	IRAS22570+5912	22:59:06.5	+59:28:28	0.12	0.15	-46.7	0	2	4
166	IRAS23151+5912	23:17:21.0	+59:28:49	0.01	0.10	-54.4	0	0	4
167	IRAS22528+5936	22:54:49.9	+59:52:49	0.55	0.03	-53.5	0.8	14.0	0	1	2
168	IRAS23032+5937	23:05:23.1	+59:53:53	0.01	0.02	-51.6	1.5	162.0	0	1	2
169	IRAS22506+5944	22:52:38.6	+60:00:56	0.95	0.03	-51.3	1.5	22.0	0	2	2
170	IRAS23138+5945	23:16:04.8	+60:01:60	0.12	0.49	-43.0	1.1	13.0	1	1	2
171	IRAS23033+5951	23:05:25.2	+60:08:12	0.10	0.04	-52.4	1.7	57.0	0	1	2
172	IRAS23133+6050	23:15:31.5	+61:07:09	0.63	0.31	-57.8	1.2	59.0	0	0	2
173	IRAS23103+6109	23:12:29.7	+61:25:36	-0.10	0.38	-55.0	1.3	11.0	0	1	2
174	IRAS23011+6126	23:03:13.1	+61:42:26	1.95	...	-10.7	1.4	33.0	0	1	2
175	Cep-A	22:56:18.9	+62:01:44	4.67	0.10	-11.1	3.5	21.6	0	1	1
176	IRAS22453+6146	22:47:17.6	+62:01:58	2.70	0.03	-10.4	1.0	42.0	0	2	2
177	IRAS23037+6213	23:05:49.0	+62:29:02	4.06	0.01	-9.8	1.1	24.0	0	1	2
178	IRAS22517+6215	22:53:40.5	+62:31:59	2.07	0.17	-8.9	0.9	73.0	0	1	2
179	IRAS22551+6221	22:57:05.2	+62:37:44	2.13	0.64	-13.4	0	0	4
180	IRAS23545+6508	23:57:05.2	+65:25:11	2.85	...	-18.4	0	0	4

^aFlag 0 means not detected; 1 means detected^bFlag 0 means not detected; 1 means detected; 2 means newly detected^cColumn ref. symbol meanings: 1—(MacDonald et al. 1981);2—(Harju et al. 1993);3—(Schreyer et al. 1996);4—(Sridharan et al. 2002)

Table 3 H₂CO parameters

Number	Source	V_{LSR} ($km\ s^{-1}$)	ΔV ($km\ s^{-1}$)	T_{MB} (K)	$N[H_2CO]$ ($10^{13} cm^{-2}$)
001	00338+6312	-17.8(0.1)	2.5(0.2)	-0.17(0.02)	4.25
003	01194+6136	-14.1(0.1)	3.2(0.4)	-0.14(0.02)	3.70
004	02219+6152	-39.9(0.1)	4.0(0.1)	-0.82(0.02)	3.22
004	02219+6152 ^b	-21.6(0.1)	1.2(0.2)	-0.12(0.02)	0.15
005	02230+6202	-43.3(0.1)	2.8(0.1)	-0.28(0.02)	1.62
006	02232+6138	-47.5(0.2)	4.8(0.6)	-0.09(0.02)	1.77
007	02244+6117	-49.6(0.1)	3.9(0.1)	-0.26(0.01)	5.34
008	02575+6017	-38.7(0.2)	1.7(0.3)	-0.06(0.02)	0.87
009	02593+6016	-38.0(0.2)	2.2(0.4)	-0.05(0.01)	0.91
013	03236+5836	-12.9(0.1)	2.6(0.2)	-0.22(0.02)	5.74
014	GGD2-3	6.5(0.1)	2.7(0.2)	-0.25(0.02)	...
015	03260+3111	8.0(0.2)	1.9(0.3)	-0.20(0.03)	...
017	04073+5102	-25.9(0.1)	1.7(0.2)	-0.12(0.02)	0.81
018	04269+3510	-6.6(0.2)	1.6(0.5)	-0.03(0.01)	0.39
019	04324+5106	-35.7(0.1)	3.8(0.3)	-0.11(0.01)	3.76
019	04324+5106 ^b	-1.2(0.5)	9.0(1.0)	-0.05(0.01)	3.18
020	04329+5047	-0.3(0.1)	1.9(0.1)	-0.12(0.01)	2.00
020	04329+5047 ^b	-37.8(0.2)	2.3(0.3)	-0.05(0.01)	0.95
021	05100+3723	-9.6(0.2)	1.8(0.4)	-0.06(0.02)	0.86
023	05274+3345	-3.4(0.1)	3.2(0.3)	-0.11(0.02)	3.07
025	05302-0537	8.5(0.1)	1.7(0.1)	-0.25(0.02)	...
027	05327-0457	11.2(0.1)	2.2(0.3)	-0.12(0.02)	...
028	05334-0611	7.9(0.1)	3.1(0.1)	-0.34(0.02)	...
029	05338-0624	7.1(0.1)	4.4(0.1)	-0.32(0.02)	...
030	05340-0603	7.2(0.2)	1.5(0.5)	-0.14(0.02)	1.99
032	05345+3157	-17.9(0.2)	3.1(0.5)	-0.06(0.02)	2.00
033	05363-0702	3.9(0.1)	2.6(0.1)	-0.35(0.02)	...
035	05358+3543	-17.4(0.1)	3.9(0.1)	-0.15(0.01)	5.68
036	05375-0731	4.4(0.1)	2.3(0.1)	-0.72(0.02)	...
037	05378-0750	4.7(0.1)	2.5(0.1)	-0.48(0.01)	14.68
038	GGD4	2.5(0.1)	2.2(0.1)	-0.28(0.02)	6.52
039	S235	-16.8(0.1)	2.8(0.3)	-0.12(0.02)	2.94
039	S235 ^b	-10.8(0.3)	3.7(0.5)	-0.06(0.02)	2.07
040	GGD7	4.8(0.1)	1.7(0.1)	-0.49(0.02)	10.44
041	05387-0149	9.6(0.2)	3.5(0.4)	-0.11(0.02)	1.98
042	05389-0756	4.9(0.1)	2.3(0.1)	-0.77(0.02)	27.34
043	05391-0217	10.3(0.1)	2.2(0.2)	-0.20(0.03)	...
044	05393-0156	9.0(0.1)	2.0(0.1)	-1.51(0.04)	3.48
046	05404-0948	2.7(0.1)	1.1(0.1)	-0.23(0.02)	2.53
047	05405-0117	9.2(0.1)	1.7(0.2)	-0.23(0.03)	3.87
047	05405-0117 ^b	2.6(0.1)	3.2(0.3)	-0.18(0.03)	5.83
048	05413-0104	4.9(0.4)	4.6(0.9)	-0.05(0.02)	2.08
050	05437-0001	10.7(0.1)	1.7(0.1)	-0.18(0.02)	...
051	05450+0019	9.5(0.1)	2.6(0.1)	-0.42(0.02)	...
052	05480+2545	-9.0(0.1)	2.2(0.1)	-0.17(0.01)	3.58
053	05490+2658	0.5(0.3)	3.1(0.5)	-0.05(0.01)	1.34
055	06006+3015	-6.4(0.2)	4.2(0.5)	-0.09(0.02)	3.27
057	Mon-R2	9.0(0.1)	4.4(0.1)	-0.29(0.02)	...
058	06055+2039	8.4(0.1)	3.6(0.1)	-0.26(0.01)	8.35
059	06056+2131	2.3(0.2)	1.2(0.4)	-0.09(0.03)	1.02
060	06061+2151	0.8(0.1)	4.3(0.2)	-0.15(0.02)	6.49
064	GGD12-15	10.6(0.1)	2.2(0.2)	-0.18(0.02)	...
065	GGD16-17	11.6(0.1)	2.3(0.2)	-0.15(0.01)	2.99
066	06105+1756	8.0(0.2)	3.0(0.3)	-0.09(0.02)	2.51
067	06114+1745	7.5(0.1)	2.3(0.1)	-0.20(0.02)	4.67
068	06117+1350	16.7(0.2)	2.1(0.3)	-0.08(0.02)	1.43
070	06308+0402	16.0(0.2)	1.7(0.5)	-0.08(0.02)	1.09
071	ROSETTE-IRS	12.0(0.1)	2.9(0.1)	-0.28(0.01)	7.75
072	06380+0949	4.8(0.1)	1.9(0.3)	-0.18(0.03)	3.22
073	06384+0932	6.3(0.1)	3.9(0.1)	-0.49(0.03)	20.99
075	06567-0355	25.6(0.2)	2.9(0.4)	-0.08(0.01)	1.89
076	06581-0848	39.0(0.2)	2.6(0.3)	-0.09(0.02)	2.34
081	18090-1832	96.9(0.2)	2.9(0.4)	-0.06(0.01)	0.76
082	18102-1800	21.2(0.1)	2.2(0.2)	-0.18(0.02)	1.45
082	18102-1800 ^b	52.9(0.2)	4.0(0.3)	-0.15(0.02)	2.20
082	18102-1800 ^c	34.2(0.2)	3.1(0.4)	-0.11(0.02)	1.21
082	18102-1800 ^d	46.4(0.3)	3.5(0.6)	-0.08(0.02)	1.05
083	18089-1732	17.8(0.1)	3.2(0.2)	-0.18(0.02)	3.97

Table 3—Continued

Number	Source	V_{LSR} ($km\ s^{-1}$)	ΔV ($km\ s^{-1}$)	T_{MB} (K)	$N[H_2CO]$ ($10^{13} cm^{-2}$)
083	18089-1732 ^b	31.2(0.1)	4.1(0.3)	-0.17(0.02)	4.51
084	18159-1550	30.4(0.2)	2.4(0.4)	-0.08(0.02)	0.97
086	18182-1433	58.3(0.2)	2.8(0.4)	-0.11(0.02)	1.72
087	18223-1243	44.7(0.4)	6.0(1.2)	-0.09(0.02)	2.45
089	18264-1152	43.9(0.1)	4.5(0.3)	-0.11(0.01)	2.76
089	18264-1152 ^b	24.0(0.1)	1.5(0.2)	-0.08(0.01)	0.75
091	18290-0924	82.3(0.4)	7.0(1.0)	-0.08(0.02)	2.55
092	18308-0841	93.3(0.2)	5.1(0.4)	-0.15(0.03)	3.79
093	18310-0825	86.3(0.3)	9.6(0.6)	-0.14(0.02)	4.72
093	18310-0825 ^b	53.3(0.3)	5.8(0.7)	-0.09(0.02)	1.93
094	G23.95+0.15	80.3(0.1)	3.1(0.2)	-0.22(0.03)	2.92
094	G23.95+0.15 ^b	108.3(0.3)	6.5(0.7)	-0.11(0.03)	3.15
094	G23.95+0.15 ^c	52.3(0.4)	6.8(1.0)	-0.08(0.03)	2.37
095	18337-0743	56.0(0.1)	7.1(0.3)	-0.23(0.02)	5.68
095	18337-0743 ^b	45.6(0.1)	2.3(0.4)	-0.12(0.02)	1.00
096	G24.49-0.04	47.8(0.2)	9.4(0.5)	-0.12(0.02)	4.17
096	G24.49-0.04 ^b	112.0(0.5)	11.0(0.9)	-0.06(0.02)	2.28
097	G24.8+0.1	108.2(0.1)	6.3(0.3)	-0.22(0.02)	3.84
097	G24.8+0.1 ^b	51.8(0.1)	3.4(0.3)	-0.15(0.02)	1.52
097	G24.8+0.1 ^c	47.2(0.1)	1.8(0.2)	-0.12(0.02)	0.67
099	18348-0616	110.2(0.2)	4.2(0.3)	-0.12(0.02)	1.48
100	18372-0541	99.2(0.4)	3.2(1.8)	-0.08(0.03)	1.03
102	G28.86+0.07	80.6(0.1)	2.8(0.3)	-0.17(0.03)	2.02
102	G28.86+0.07 ^b	99.6(0.3)	4.2(0.6)	-0.11(0.03)	1.97
104	18460-0307	83.5(0.1)	3.0(0.2)	-0.20(0.03)	3.91
105	W43S	99.6(0.1)	7.2(0.3)	-0.42(0.03)	7.10
105	W43S ^b	7.0(0.2)	2.7(0.3)	-0.18(0.03)	1.14
105	W43S ^c	49.7(0.2)	2.4(0.3)	-0.17(0.03)	0.91
106	18447-0229	104.0(0.1)	2.8(0.2)	-0.17(0.02)	1.39
106	18447-0229 ^b	49.5(0.2)	3.7(0.7)	-0.08(0.02)	0.84
107	18437-0216	96.2(0.2)	4.2(0.3)	-0.15(0.02)	2.40
108	18426-0204	15.7(0.2)	3.8(0.5)	-0.08(0.02)	1.56
108	18426-0204 ^b	44.2(0.2)	1.8(0.4)	-0.08(0.02)	0.68
108	18426-0204 ^c	92.1(0.3)	4.6(0.9)	-0.05(0.02)	1.31
109	18454-0158	93.6(0.5)	8.2(0.5)	-0.72(0.02)	11.51
109	18454-0158 ^b	82.3(0.5)	3.1(0.5)	-0.17(0.02)	0.95
109	18454-0158 ^c	12.2(0.5)	4.9(0.5)	-0.08(0.02)	0.65
110	18440-0148	97.1(0.1)	5.7(0.2)	-0.25(0.02)	5.07
110	18440-0148 ^b	81.8(0.2)	5.4(0.6)	-0.11(0.02)	2.20
110	18440-0148 ^c	60.0(0.2)	2.5(0.4)	-0.06(0.02)	0.61
111	18454-0136	104.7(0.4)	10.1(0.6)	-0.09(0.02)	3.05
111	18454-0136 ^b	77.9(0.2)	10.2(0.3)	-0.09(0.02)	2.76
111	18454-0136 ^c	41.1(0.3)	7.9(0.9)	-0.06(0.02)	1.56
111	18454-0136 ^d	12.5(0.2)	2.1(0.6)	-0.06(0.02)	0.41
112	G31.4-0.3	96.6(0.1)	6.2(0.2)	-0.26(0.02)	8.88
113	18488+0000	99.4(0.2)	2.5(0.5)	-0.08(0.02)	0.84
113	18488+0000 ^b	83.1(0.2)	2.1(0.5)	-0.05(0.02)	0.54
116	18502+0051	106.4(0.2)	4.4(0.5)	-0.09(0.02)	2.23
117	W48	43.3(0.1)	4.0(0.1)	-0.49(0.02)	5.65
118	S68	7.8(0.1)	2.2(0.1)	-0.37(0.02)	...
119	G34.3+0.1	59.3(0.1)	5.8(0.1)	-0.57(0.02)	9.70
121	18515+0157	51.6(0.1)	4.2(0.3)	-0.17(0.02)	4.36
121	18515+0157 ^b	13.8(0.1)	1.5(0.2)	-0.12(0.02)	1.03
121	18515+0157 ^c	43.8(0.2)	3.2(0.5)	-0.09(0.02)	1.82
122	18530+0215	14.1(0.1)	2.1(0.2)	-0.23(0.02)	2.35
122	18530+0215 ^b	77.9(0.3)	7.8(0.6)	-0.11(0.02)	3.92
123	18540+0220	28.9(0.1)	1.5(0.3)	-0.12(0.01)	0.78
123	18540+0220 ^b	13.3(0.2)	3.1(0.4)	-0.08(0.01)	0.97
123	18540+0220 ^c	19.4(0.2)	1.5(0.3)	-0.05(0.01)	0.28
124	18566+0408	85.2(0.1)	5.1(0.3)	-0.17(0.02)	4.09
124	18566+0408 ^b	18.3(0.1)	1.6(0.3)	-0.11(0.02)	0.87
125	18553+0414	20.5(0.1)	1.5(0.2)	-0.11(0.02)	1.01
129	S76E	28.8(0.1)	5.1(0.1)	-0.45(0.02)	12.90
130	19074+0752	68.0(0.3)	3.9(0.6)	-0.08(0.02)	1.96
131	G45.49+0.13	59.3(0.1)	5.6(0.4)	-0.31(0.04)	7.63
132	19175+1357	9.6(0.4)	8.7(1.0)	-0.06(0.02)	2.69
133	19220+1432	68.0(0.4)	5.4(0.8)	-0.06(0.02)	1.82
134	19217+1651	2.7(0.1)	4.9(0.4)	-0.09(0.01)	3.41

Table 3—Continued

Number	Source	V_{LSR} ($km\ s^{-1}$)	ΔV ($km\ s^{-1}$)	T_{MB} (K)	$N[H_2CO]$ ($10^{13} cm^{-2}$)
135	19266+1745	21.0(0.1)	2.1(0.3)	-0.11(0.02)	1.63
135	19266+1745 ^b	4.1(0.2)	3.5(0.6)	-0.06(0.02)	1.53
136	19282+1814	24.1(0.1)	2.1(0.2)	-0.11(0.01)	1.60
138	19411+2306	28.3(0.3)	4.7(0.6)	-0.06(0.02)	2.00
139	19413+2332	21.5(0.2)	3.7(0.4)	-0.09(0.02)	2.93
140	S87	25.0(0.2)	1.1(0.3)	-0.06(0.02)	0.46
141	S88	21.8(0.1)	2.9(0.2)	-0.17(0.02)	2.47
142	19471+2641	19.9(0.3)	4.6(0.6)	-0.05(0.02)	1.44
143	20081+2720	4.7(0.1)	1.9(0.2)	-0.18(0.02)	3.42
144	ON1	10.4(0.1)	4.1(0.2)	-0.20(0.01)	8.16
145	20051+3435	10.1(0.2)	2.7(0.4)	-0.08(0.02)	1.69
146	S106	-1.2(0.1)	3.5(0.3)	-0.11(0.01)	1.22
147	ON2	-1.0(0.2)	6.8(0.4)	-0.20(0.03)	5.68
148	20205+3948	-0.5(0.1)	2.0(0.1)	-0.32(0.01)	2.56
149	20293+3952	3.5(0.1)	2.6(0.4)	-0.15(0.02)	2.12
149	20293+3952 ^b	9.3(0.4)	6.3(1.2)	-0.08(0.02)	2.43
150	20275+4001	0.3(0.1)	2.0(0.1)	-0.20(0.01)	1.83
150	20275+4001 ^b	-5.9(0.2)	2.8(0.4)	-0.06(0.01)	0.80
152	20216+4107	11.2(0.1)	3.4(0.2)	-0.14(0.02)	2.29
153	R131	4.9(0.1)	2.5(0.1)	-0.28(0.01)	4.31
154	20319+3958	-0.1(0.2)	1.6(0.5)	-0.08(0.02)	0.71
156	20343+4129	5.1(0.3)	3.0(0.5)	-0.08(0.02)	0.80
157	22308+5812	-52.7(0.1)	2.5(0.3)	-0.08(0.01)	1.46
158	22444+5827	-4.0(0.1)	1.4(0.1)	-0.15(0.01)	2.00
159	22134+5834	18.5(0.2)	3.1(0.4)	-0.06(0.01)	1.51
160	22267+6244	-3.2(0.2)	3.1(0.3)	-0.11(0.02)	3.04
161	S140	-8.3(0.1)	2.7(0.2)	-0.17(0.02)	4.25
162	R146	-10.5(0.1)	1.9(0.2)	-0.12(0.01)	...
163	22539+5758	-54.7(0.2)	2.9(0.4)	-0.06(0.02)	1.77
164	22566+5830	-51.3(0.1)	3.4(0.1)	-0.23(0.01)	6.23
165	22570+5912	-47.2(0.3)	4.0(0.5)	-0.06(0.02)	1.76
167	22528+5936	-53.8(0.1)	2.0(0.3)	-0.05(0.01)	0.96
168	23032+5937	-51.9(0.1)	3.0(0.2)	-0.22(0.02)	6.30
169	22506+5944	-52.4(0.3)	2.7(0.6)	-0.05(0.02)	1.29
170	23138+5945	-43.9(0.2)	1.4(0.4)	-0.06(0.02)	0.55
170	23138+5945 ^b	-41.1(0.2)	1.6(0.4)	-0.06(0.02)	0.58
171	23033+5951	-52.4(0.1)	3.6(0.2)	-0.22(0.02)	7.75
173	23103+6109	-56.4(0.1)	6.1(0.2)	-0.23(0.02)	9.93
174	23011+6126	-11.0(0.1)	2.4(0.2)	-0.18(0.02)	4.54
175	Cep-A	-11.1(0.1)	2.7(0.4)	-0.15(0.03)	3.68
176	22453+6146	-11.2(0.1)	2.0(0.2)	-0.15(0.02)	2.89
177	23037+6213	-10.6(0.1)	2.3(0.1)	-0.38(0.02)	9.79
178	22517+6215	-10.0(0.1)	2.1(0.2)	-0.14(0.02)	2.33

Table 4 H110_α parameters

Number	Source	V_{LSR} ($km\ s^{-1}$)	ΔV ($km\ s^{-1}$)	T_{MB} (K)
002	00494+5617	-25.8	21.5	0.04
005	02230+6202	-45.8	27.9	0.16
006	02232+6138	-42.5	23.9	0.04
007	02244+6117	-47.9	30.6	0.02
016	03595+5110	-25.7	23.9	0.07
017	04073+5102	-50.7	26.3	0.07
026	05327-0529	-5.4	29.7	1.28
041	05387-0149	3.8	22.3	0.06
044	05393-0156	4.7	18.2	0.37
057	MON R2	12.5	37.3	0.05
062	06068+2030	6.4	26.4	0.05
082	18102-1800	33.1	16.9	0.08
085	18151-1208	26.9	26.0	0.05
091	18290-0924	85.2	26.1	0.04
093	18310-0825	91.1	16.3	0.08
095	18337-0743	92.9	13.4	0.05
096	G24.49-0.04	104.5	44.7	0.06
099	18348-0616	108.6	28.4	0.11
105	W43S	95.8	24.6	0.23
106	18447-0229	101.0	22.4	0.11
107	18437-0216	105.4	24.2	0.04
109	18454-0158	97.0	33.8	0.26
110	18440-0148	100.7	31.7	0.03
113	18488+0000	98.6	27.2	0.03
117	W48	46.1	21.9	0.13
119	G34.3+0.1	54.1	26.4	0.15
123	18540+0220	51.4	22.9	0.08
129	S76E	24.2	21.2	0.06
131	G45.49+0.13	56.9	23.5	0.08
132	19175+1357	10.2	17.0	0.04
133	19220+1432	59.6	34.4	0.04
141	S88	29.5	25.1	0.06
142	19471+2641	15.7	22.8	0.04
147	ON2	-8.6	32.9	0.09
150	20275+4001	10.3	38.2	0.04
170	23138+5945	-45.4	28.3	0.03

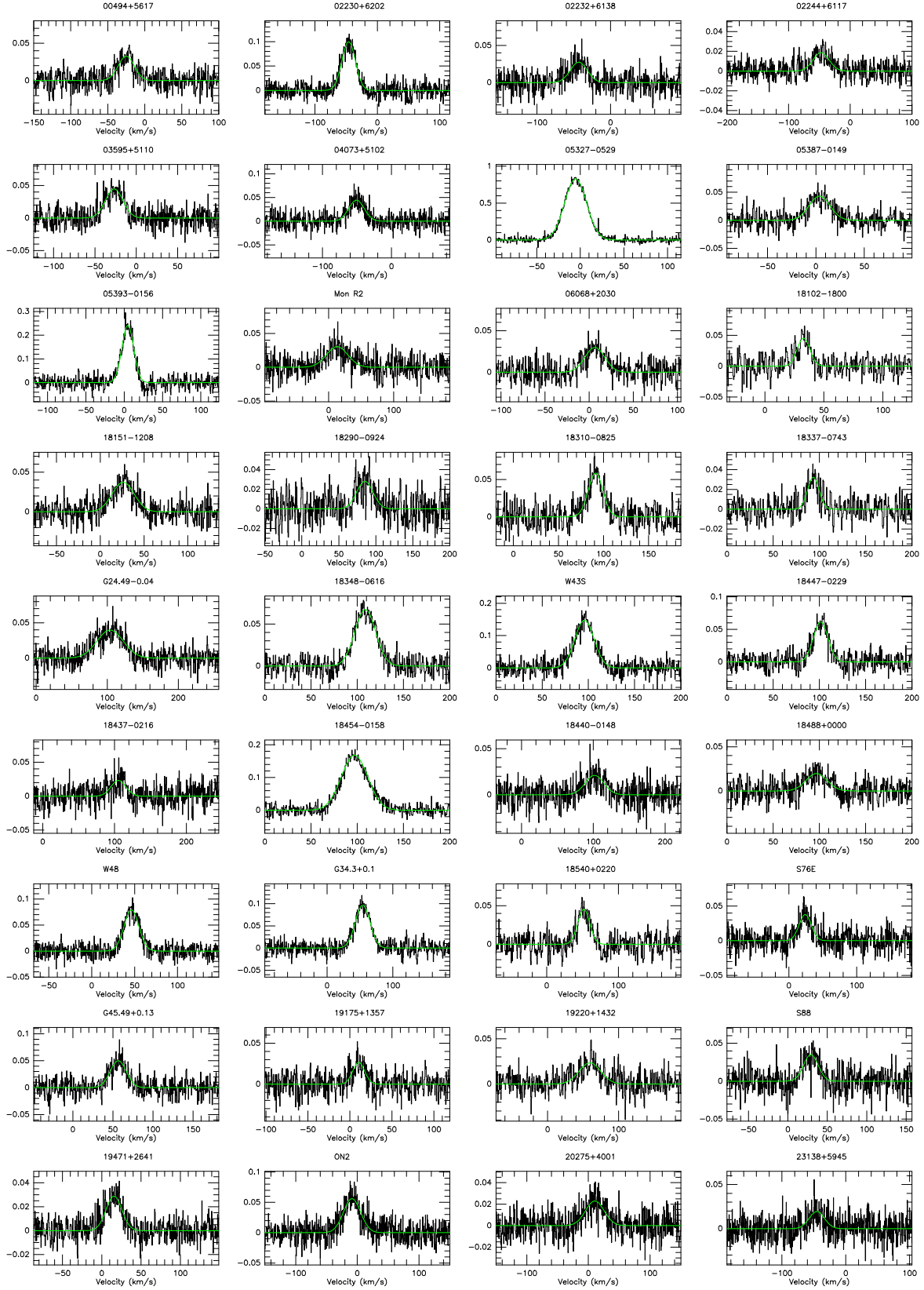


Fig. 12 Detected RRL lines (intensity in T_A^*).

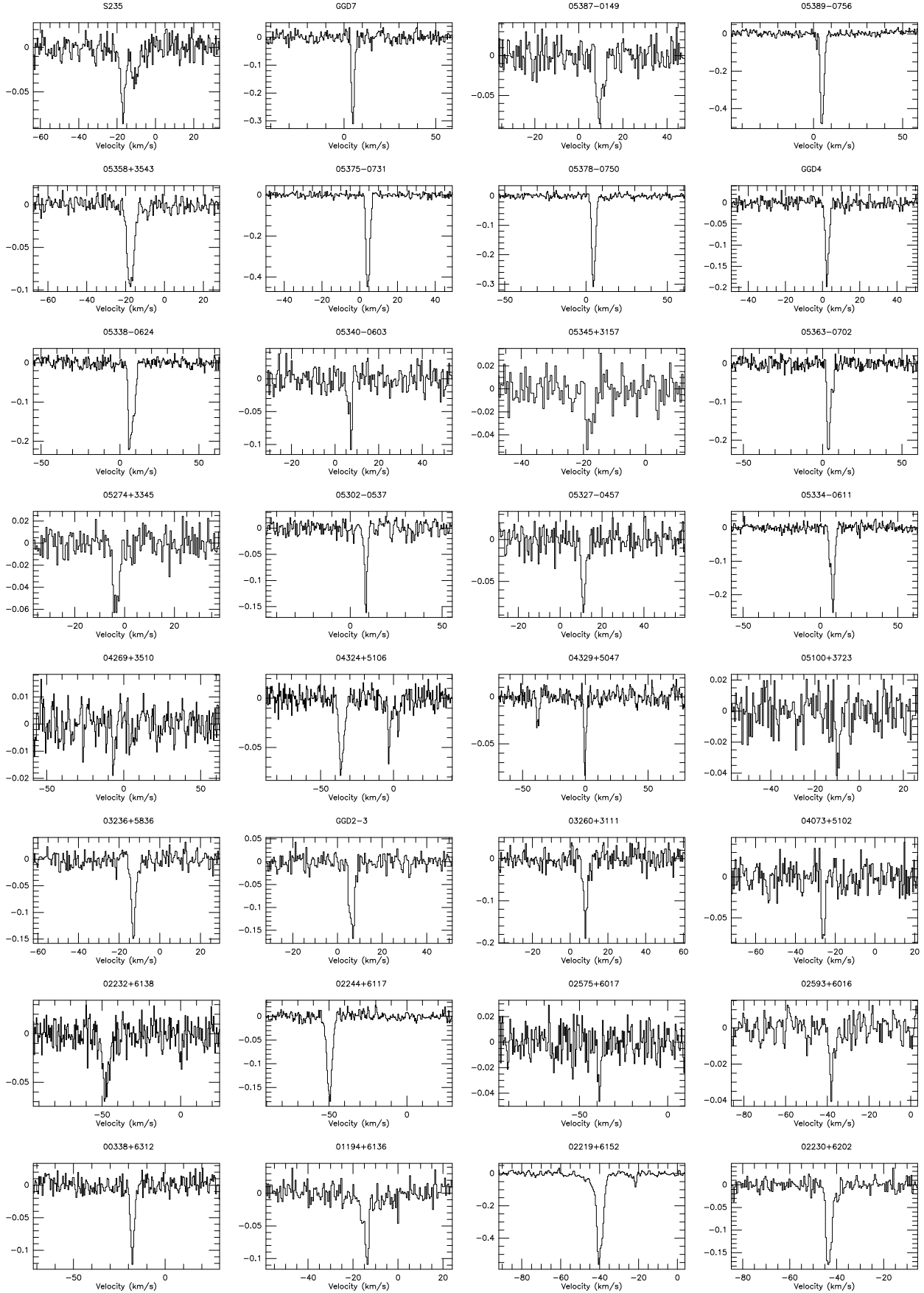


Fig. 13 Sources detected with H_2CO (intensity in T_A^*).

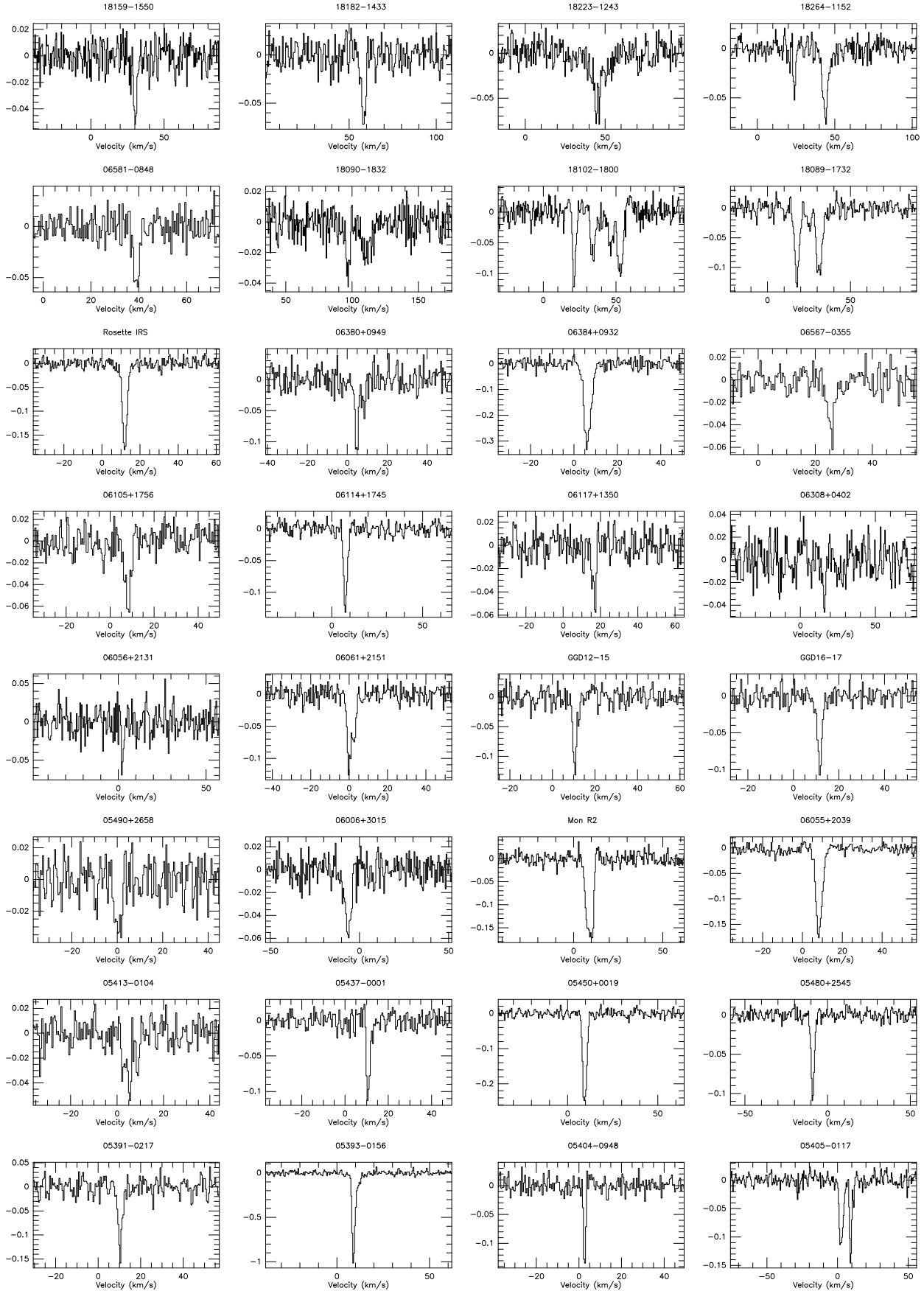


Fig. 13 Continued

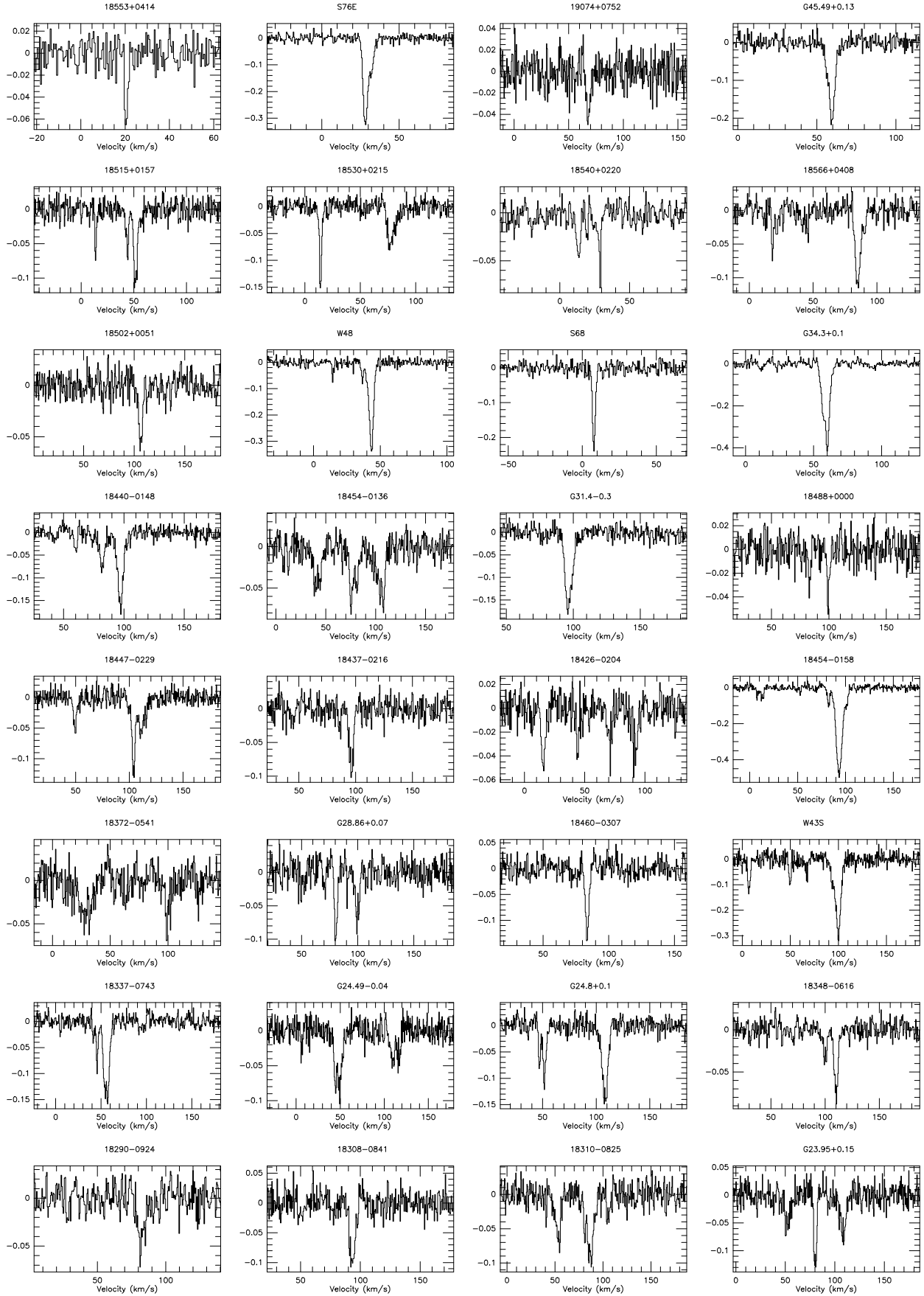


Fig. 13 Continued

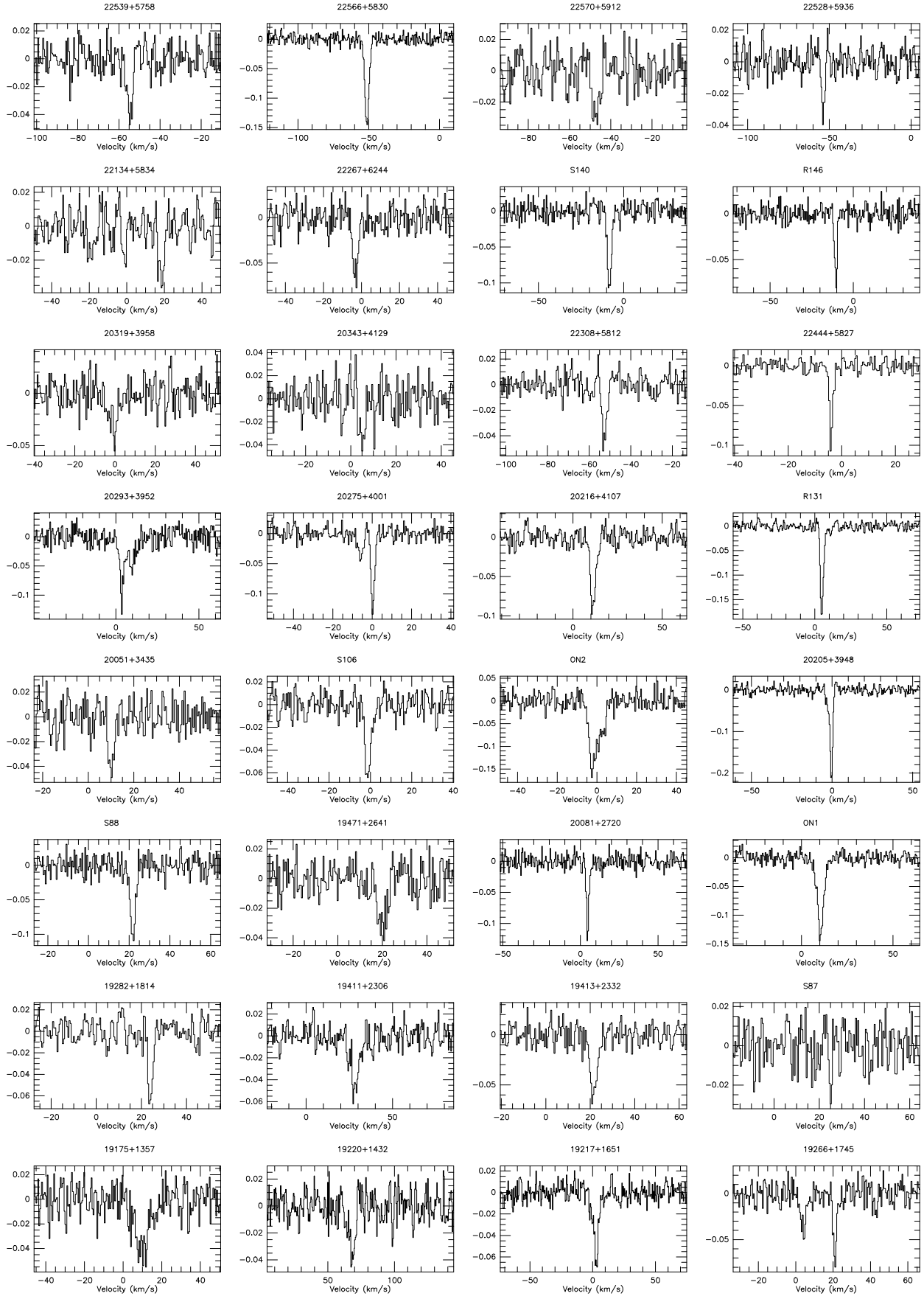


Fig. 13 Continued

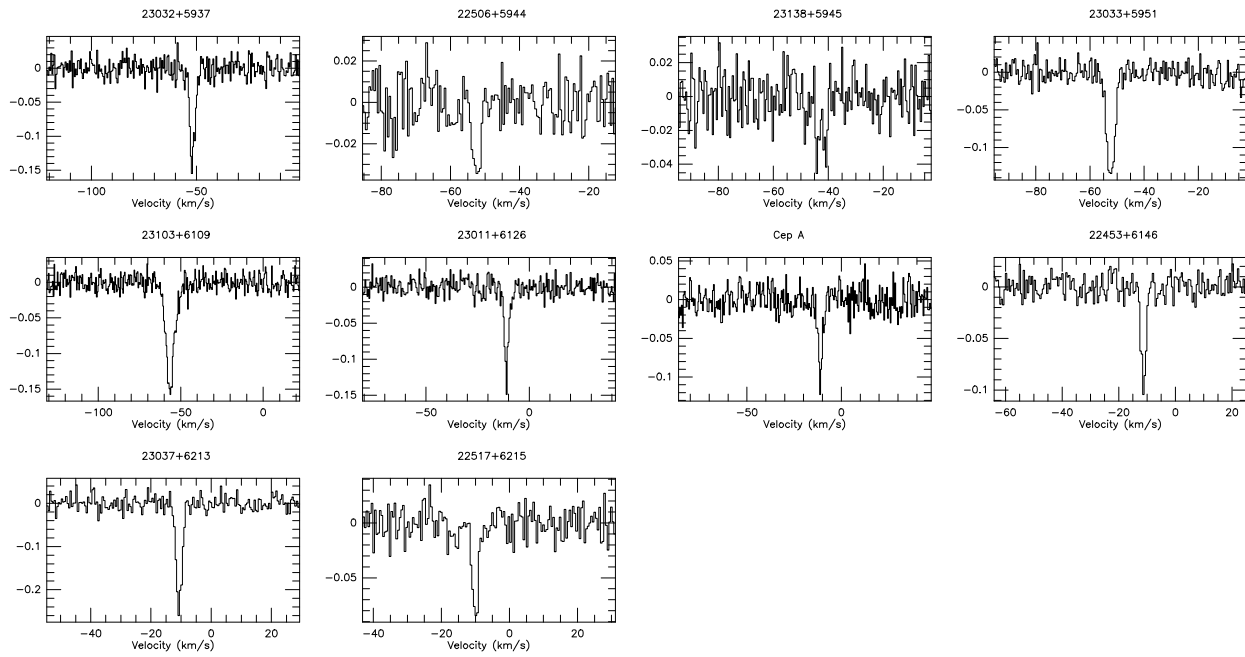


Fig. 13 Continued

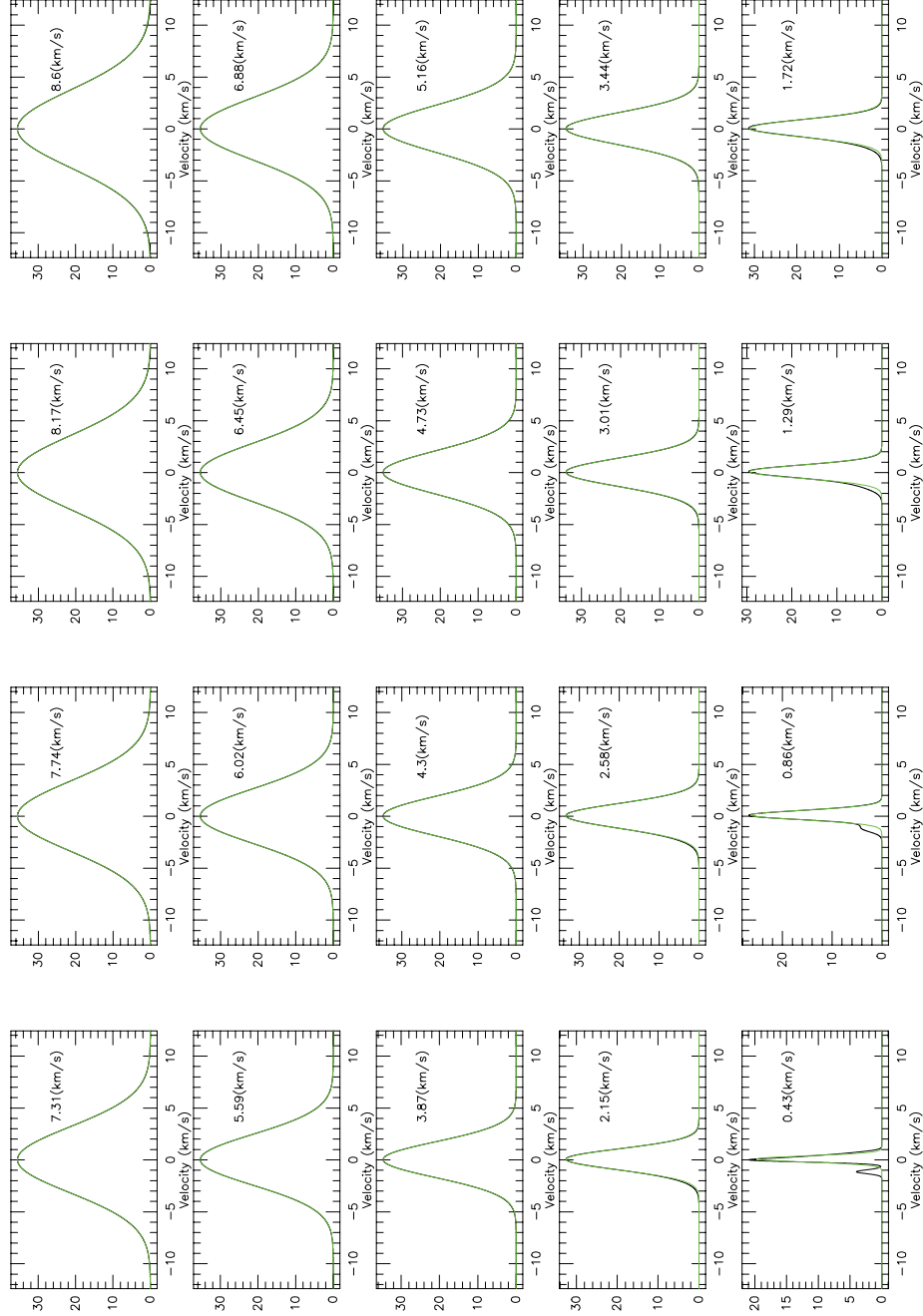


Fig. 14 Blended HFS simulation of H_2CO . The blended spectra of five HFS components are plotted in *black lines* and the gaussian fittings are in *green line*.